Journal of Marine Science and Application (2026) 25: 1294-1317
https://doi.org/10.1007/s11804-026-00835-4

RESEARCH ARTICLE

A Coupled Dynamic Model of the Floating Offshore Wind Turbine with Mass Dampers Considering Rotational Displacement Magnitude

Shujin Li[1,2], Yuan Zhao[1,2], Ruibo Wang[1] and Irakoze Jean Paul[1]

Received: 06 May 2025 / Accepted: 18 March 2026
© Harbin Engineering University and Springer-Verlag GmbH Germany, part of Springer Nature 2026

Abstract

As a multi-body system, the floating offshore wind turbine (FOWT) exhibits significant coupling effect between rotational and translational displacements, and neglecting some rotational angles or applying small-angle assumption in calculations will influence the accuracy of results. In this paper, a 16 degrees of freedom multi-body coupled model including platform, tower, and rotor blades is established. The model fully accounts for coordinate transformations caused by FOWT's rotation without small-angle assumption, while considering the coupling characteristics between aerodynamic forces, hydrodynamic forces, and structure, and is employed for calculating FOWT responses and investigating the control performance of mass dampers. Taking the Spar-type FOWT as an example, the simulation results comparison between the coupled model and OpenFAST demonstrates its accuracy. Subsequent response analysis indicates that the small-angle assumption underestimates the FOWT response under free vibration and wave loading, while overestimating response under wind loading. Simultaneously, the impact of hydrodynamic computational methods and servo control systems on the calculation results was also analyzed. Finally, using tuned swing mass damper as an example, the modeling method for mass dampers is introduced and the impact of small-angle assumption on computational results is analyzed, providing reference for researchers in the field of FOWT control.

Keywords Floating offshore wind turbine; Multi-body system; Aerodynamic analysis; Hydrodynamic analysis; Coupled model

1 Introduction

The acceleration of global industrialization has made clean energy increasingly important for the economic development and environmental sustainability. As a common and easy-to-develop clean renewable energy, wind energy has a great significance to be actively developed and utilized, which can improve the energy mix and the environment (Cacciuttolo et al., 2024; Hannan et al., 2023; Olabi et al., 2023). Compared to onshore and near-offshore wind power, deep-sea wind power has the advantages of the abundant wind resources, stable wind speeds, and suitability for large-scale equipment, which has become the main direction of the wind energy utilization today (Ramakrishnan et al., 2024; Su et al., 2024).

With the increase of the water depth, due to the difficulty and high cost of the traditional fixed foundation wind turbine in construction, the floating offshore wind turbine (FOWT) becomes a reasonable choice for the deep-sea wind power (Edwards et al., 2023; Edwards et al., 2024). Compared to the fixed wind turbine, the offshore floating wind turbine has a more complex ensemble structure including special components such as floating platform and mooring cables, which make it a complex multi-body system. Under variable environmental loads such as wind, waves, and ocean currents, the responses of different components of the FOWT are coupled with each other, which results in complex movements and brings more difficulties in the calculation and simulation (Ojo et al., 2022; Zhang et al., 2024; Evro et al., 2025). To ensure the safety and reliability of the FOWT, it is necessary to consider the coupled model of the FOWT under multiple environmental loads and calculate its system response accurately.

Various types of floating platforms of the FOWT have been developed under different environmental conditions, mainly including Spar, Tension-leg, Barge, and Semi-sub-

Article Highlights

- A high-fidelity coupled dynamic model is established to solve the motion response of FOWT.
- The strict transformation matrix is employed to describe rotational motion of multi-body system.
- The impact of small angle assumption on responses calculation of FOWT is analyzed.
- The influence of small angle assumption on damper's response and control effect is evaluated.

✉ Yuan Zhao
zhaoyuan_work@163.com

[1] School of Civil Engineering and Architecture, Wuhan University of Technology, Wuhan 430070, China

[2] Sanya Science and Education Innovation Park of Wuhan University of Technology, Sanya 572025, China

mersible (Jonkman and Matha, 2010; Pérez-Collazo et al., 2015). Some software or modeling frameworks have been applied to establish FOWT multibody models, such as OpenFAST (Jonkman and Buhl, 2005), HAWC2 (Larsen and Hansen, 2014), Bladed (DNV GL, 2016), FLEX5 (Høeg and Zhang, 2021), SIMO/RIFLEX (Ormberg et al., 2011), and SIMPACK (Xie et al., 2025). However, when researchers consider installing mass dampers within the FOWT to suppress its response, the aforementioned software may not be convenient for modeling. The researchers often established new model based on relevant parameters to ensure that mass dampers with different mechanical models achieve optimal control performance (López-Queija et al., 2022; Tian et al., 2023).

According to different control objectives, some researchers have developed simple or complex dynamic models for the FOWT. Al-Solihat et al. (2019) established a simplified 7 degrees of freedom (DOFs) dynamic model for the Spar FOWT without using the small-angle assumption, considering 6-DOF of the platform and generator speed. Chen et al. (2019) and Wang et al. (2025) developed an in-house aero-hydro-elastic-mooring-servo coupled time-domain solver for FOWT, applied to the performance analysis and optimization of passive gyrostabilizers. Jahangiri and Sun (2020) established a 13-DOF coupling model for the Spar FOWT, which considered the coupling effect among blades, tower, and platform. Further, a 14-DOF coupling model for the Spar FOWT established by Yang and He (2020), and considered the platform yaw additionally, to control the rotor speed and pitch response. Besides, Høeg and Zhang (2021) proposed a partially linearized 17-DOF coupled dynamic model for the FOWT with the small-angle assumption, additionally considering the DOFs of the tower torsion, the drivetrain and generator, compared with the 14-DOF model (Yang and He, 2020). Based on the vortex-induced vibration problem in FOWT, Mu et al. (2022) have proposed a computational fluid dynamics model based on nesting grid technology, aiming to achieve a fully coupled fluid-structure interaction numerical analysis of the bluff body platform. Zhang (2022) optimized the proposed electromagnetic shunt tuned mass damper using a reduced-order in-plane motion model, subsequently evaluating its time-domain performance using the 17-DOF FOWT model. Falcão et al. (2023) developed a 6-DOF coupled model incorporating an inverted pendulum tuned mass damper to control the response of the Barge-type FOWT under wind loads. Zuo et al. (2023) modelled the blades and tower of the spar-type FOWT using three-dimensional Euler-Bernoulli beam elements, and established a 498-DOF motion equation taking into account their distributed mass and stiffness. Yu et al. (2023) developed a numerical aero-hydro-servo-elastic model coupling a tuned liquid column damper with a FOWT which is simplified and linearized, and the comparison of experimental and numerical results demonstrates that the coupled model can effectively simulate the system's response. Luo et al. (2024) developed an analytical model for semi-submersible FOWT that accounts for the rigid-body DOF of the platform and the flexible vibration DOF of the tower and blades, and conducted research on the control of its ultra-low-frequency vibrations. Yang et al. (2025) established a 14-DOF semi-submersible FOWT model to evaluate the control performance of two-dimensional adjustable tuned mass dampers on the roll and pitch responses of FOWT under various environmental loads. Chang and Peng (2025) proposed a hybrid control device based on tuned mass damper-inerter and coupled it with a 15-DOF Spar-type FOWT model. Sun et al. (2025) have proposed a frequency-domain FOWT random response calculation method using statistical linearization to address the issue of low computational efficiency in time-domain model. Zhang et al. (2023; 2025) developed numerical and experimental models using semi-submersible FOWT as an example, and provide a technical reference for the parameter optimization and performance testing of vibration-damping devices.

In the above studies, researchers selected the FOWT models with different DOFs due to different research objectives. For example, when only considering the pitch motion of the FOWT in single direction, only 2 DOFs can meet the calculation accuracy requirement (Stewart and Lackner, 2013; Hu and He, 2017). If the research target is considering components of the FOWT such as towers or blades, the corresponding DOF cannot be ignored (Si et al., 2014; Dinh and Basu, 2015; He et al., 2019). Due to the coupling effect between each DOF, considering more DOFs enables more accurate simulation of motion response of the FOWT. However, as the DOF of the model increases, the motion equations of the FOWT will become increasingly complex, and the computational cost will also increase accordingly. In order to simplify the derivation process of the Euler-Lagrange equation and reduce the computational cost of the model, some researchers have ignored rotational displacement of some components or adopted the small-angle assumption to simplify the calculation of trigonometric functions. However, this simplification produces non-negligible errors when the FOWT rotational displacement is large. At the same time, using the small-angle assumption will lead to the coordinate transformation matrix no longer be orthogonal, resulting in additional calculation errors (Jonkman, 2009). On the other hand, in the study of FOWT response suppression, the coupling effects between each DOF and the mass damper should be fully considered. Unlike fixed structures, FOWT's rotational displacement in each direction will cause the mass damper to move along an angle-varying inclined plane, resulting in the mass damper being subjected to its own weight. Although some researchers validated the feasibility of their model by comparing the free vibration results with

OpenFAST, further research is needed to investigate the effects of the small-angle assumption on the motion of the FOWT model and related mass dampers under complex environmental loads.

In this paper, an improved 16-DOF coupling dynamic model for the Spar FOWT under complex working conditions is established, and the modeling method of mass damper setting in FOWT is explained. The following improvements are made in the model: 1) strict transformation matrix is employed to describe the conversion of motion in local coordinate systems to the global inertial coordinate system, instead of the coordinate rotation matrix simplified by small-angle assumption; 2) Using linear potential flow theory combined with Morrison equation to calculate hydrodynamics instead of the single Morrison equation; 3) the influence of the generator torque control, blade pitch control and blade deflection is considered in calculation. Based on the established model, the influence of simplifying the rotation transformation matrix using the small-angle assumption on the calculation results is further studied, and the influence of using the small-angle assumption modeling on control performance of tuned swing mass damper (TSMD) for the FOWT is also studied.

The research contents of each section of this paper are arranged as follows: In Section 2, the motion equation of the coupling model is derived through the Euler-Lagrange equation and the generator-torque control and blade-pitch control methods are introduced. In Section 3, the aerodynamic load is calculated by the modified blade element-momentum theory, and the hydrodynamic load is obtained according to the linear wave theory, which not suffers the limitation of the traditional Morison equation. At the same time, the quasi-static method is used to calculate the mooring tension. In Section 4, the comparison with calculation results of OpenFAST demonstrates the accuracy of proposed coupled model. Then, based on the established model, the FOWT responses with and without the small-angle assumption were compared and analyzed. In addition, the influence on responses of hydrodynamic forces calculated by Morrison's equation was evaluated, and the effect of generator-torque control and blade collective pitch control is analyzed using the established coupling model. In Section 5, the controlled FOWT model including TSMD (Jahangiri and Sun, 2020) is established by the proposed method, the error of the TSMD motion response caused by the small-angle assumption under different load conditions is analyzed.

2 Coupled model of the spar FOWT

The Spar FOWT consists of the turbine, tower, floating platform, and mooring system, which is regarded as a complicated multi-body system. This section aims to establish a highly-coupled dynamic model for the Spar FOWT including aerodynamics, hydrodynamics, mooring, and pitch control modules. According to the actual situation of the FOWT, the following assumptions are considered to simplify the model:

(1) The platform, nacelle, and hub are assumed as rigid bodies, respectively. The tower and blades are modeled as the flexible cantilever beam, which consider the bending deformation and ignored the axial deformation. The quasi-static approach is employed to analyze the mooring system to ignore the inertia and damping.

(2) The turbine is composed of three blades, a rotor, and a nacelle. The mass of the drivetrain and generator are integrated into the nacelle because they are located in the nacelle. The drivetrain is modeled as the linear spring and damping system, and its mechanical loss is neglected with the assumption that the gearbox efficiency is 100%. The nacelle yaw is also neglected in the study.

(3) The external excitation mainly considers aerodynamic, hydrodynamic, and hydrostatic loads, ignoring the influence of icing, currents, wake turbulence and lightning. The aerodynamic force is generated by the relative motion between the incoming wind and the blade, neglecting the influence of the wind on the tower. Hydrodynamic load is generated by the relative motion of the platform and fluid, and hydrostatic load includes buoyancy and hydrostatic restoring force.

A coupled model with 16 DOFs shown in Figure 1 for the Spar FOWT is considered in this study. $q_1, q_2, q_3, q_4, q_5, q_6$ represent the translational and rotational coordinate of the platform, denoting surge, sway, heave, roll, pitch, and yaw, respectively. q_7, q_8 denotes the tower fore-aft and side-side vibrations; $q_{10+j}, q_{13+j}, j = 1, 2, 3$ describe the blades flapwise and edgewise vibrations. Moreover, q_9, q_{10} are additionally considered as the DOFs of the drivetrain and generator in this paper. Thus, the azimuth of the blade j can be expressed as:

$$\psi_j(t) = q_9 + q_{10} + \frac{2}{3}\pi(j-1), j = 1, 2, 3 \tag{1}$$

2.1 Coordinate systems

To accurately model the floating offshore wind turbine, each component is defined in its local coordinate system and integrated into the global coordinate system. The coordinate systems of the model are defined in Figure 2. $\boldsymbol{z}_1$, $\boldsymbol{z}_2, \boldsymbol{z}_3$ represents the axes of the inertial coordinate system, where $\boldsymbol{z}_1\boldsymbol{z}_2$-plane designates the still water level (SWL), the $\boldsymbol{z}_1$-axis directs along the nominal wind direction and the $\boldsymbol{z}_3$-axis directs opposite to gravity along the center line of the undeflected tower.

Local coordinate systems include the platform/tower-base coordinate $\boldsymbol{a}_1, \boldsymbol{a}_2, \boldsymbol{a}_3$, the tower-top/nacelle coordinate $\boldsymbol{d}_1, \boldsymbol{d}_2, \boldsymbol{d}_3$, the shaft coordinate $\boldsymbol{c}_1, \boldsymbol{c}_2, \boldsymbol{c}_3$, the rotor azimuth

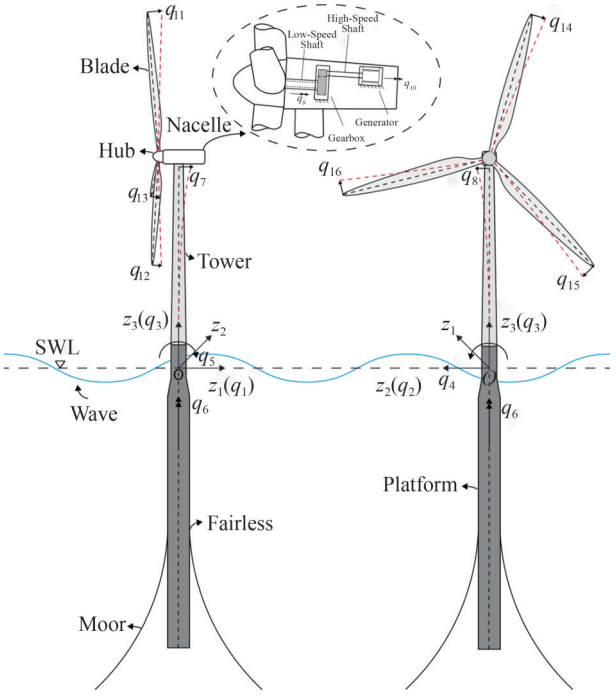


Figure 1 Model of the spar floating offshore wind turbine

coordinate $\boldsymbol{e}_1, \boldsymbol{e}_2, \boldsymbol{e}_3$, the hub coordinate $\boldsymbol{g'}^j_1, \boldsymbol{g'}^j_2, \boldsymbol{g'}^j_3$, the blade cone angle coordinate $\boldsymbol{i'}^j_1, \boldsymbol{i'}^j_2, \boldsymbol{i'}^j_3$, and the blade coordinate $\boldsymbol{j'}^j_1, \boldsymbol{j'}^j_2, \boldsymbol{j'}^j_3$.

Coordinate systems are generally transformed by coordinate rotation matrix. However, OpenFAST software uses singular-value decomposition to orthogonalize the Euler-angle transformation matrix considering the small-angle assumption with the rotation angle less than 15 degrees. In order to consider the influence of a large rotation angle, the strict coordinate rotation matrix without the small-angle assumption is used here to describe the motion of the complex multi-body system of the FOWT. In this regard, when the local coordinate rotates the Euler angle $\boldsymbol{\theta} = \{\theta_1, \theta_2, \theta_3\}$ around the x, y, z axis, the transformed coordinate X, Y, Z (Fossen, 2011) can be expressed as:

$$\begin{Bmatrix} X \\ Y \\ Z \end{Bmatrix} = \boldsymbol{R} \begin{Bmatrix} x \\ y \\ z \end{Bmatrix} = \begin{bmatrix} c_{\theta_2} c_{\theta_3} & c_{\theta_1} s_{\theta_3} + s_{\theta_1} s_{\theta_2} c_{\theta_3} & s_{\theta_1} s_{\theta_3} - c_{\theta_1} s_{\theta_2} c_{\theta_3} \\ -c_{\theta_2} s_{\theta_3} & c_{\theta_1} c_{\theta_3} - s_{\theta_1} s_{\theta_2} s_{\theta_3} & s_{\theta_1} c_{\theta_3} + c_{\theta_1} s_{\theta_2} s_{\theta_3} \\ s_{\theta_2} & -s_{\theta_1} c_{\theta_2} & c_{\theta_1} c_{\theta_2} \end{bmatrix} \begin{Bmatrix} x \\ y \\ z \end{Bmatrix} \tag{2}$$

where $s_{(\cdot)} = \sin(\cdot)$, $c_{(\cdot)} = \cos(\cdot)$.

2.2 Equation of motion

The Euler-Lagrange equation is implemented to establish the control equations of the motion of the Spar FOWT (Chopra, 2007), and it can be shown as:

$$\frac{\mathrm{d}}{\mathrm{d}t}\left(\frac{\partial T}{\partial q_i'}\right) - \left(\frac{\partial T}{\partial q_i}\right) + \left(\frac{\partial V}{\partial q_i}\right) = F_i^{\mathrm{a}} + F_i^{\mathrm{hs}} + F_i^{\mathrm{hd}} + F_i^{\mathrm{m}} + F_i^{\mathrm{g}} - C_{ij}^{\mathrm{s}} q_j' \tag{3}$$

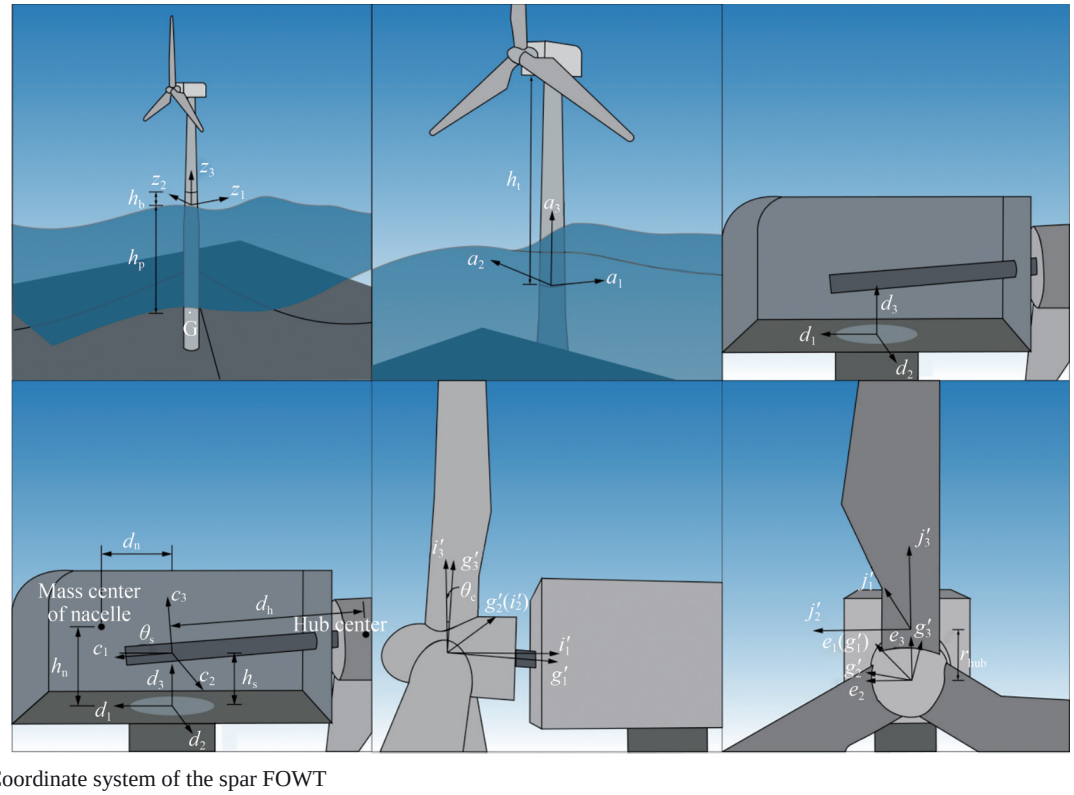


Figure 2 Coordinate system of the spar FOWT

where T and V denote the system kinetic and potential energies, respectively. q_i is the generalized coordinates, and q_i' is the derivative of q_i over time. $F_i^{\mathrm{a}}, F_i^{\mathrm{hs}}, F_i^{\mathrm{hd}}, F_i^{\mathrm{m}}, F_i^{\mathrm{g}}$ represent the aerodynamic, hydrostatic, hydrodynamic, mooring, and generator loads corresponding to the component of q_i, respectively. C_{ij}^{s} is the structural damping of the model.

The kinetic energy of the Spar FOWT can be defined as follows:

$$\begin{aligned} T = &\frac{1}{2} m_{\mathrm{p}} \boldsymbol{v}_{\mathrm{p}}^{\mathrm{T}} \boldsymbol{v}_{\mathrm{p}} + \frac{1}{2} \boldsymbol{\omega}_{\mathrm{p}}^{\mathrm{T}} \boldsymbol{J}_{\mathrm{p}} \boldsymbol{\omega}_{\mathrm{p}} + \frac{1}{2} \int_0^{h_{\mathrm{t}}} \mu_{\mathrm{t}}(h) \boldsymbol{v}_{\mathrm{t}}^{\mathrm{T}} \boldsymbol{v}_{\mathrm{t}} \mathrm{d}h + \\ &\frac{1}{2} m_{\mathrm{n}} \boldsymbol{v}_{\mathrm{n}}^{\mathrm{T}} \boldsymbol{v}_{\mathrm{n}} + \frac{1}{2} \boldsymbol{\omega}_{\mathrm{n}}^{\mathrm{T}} \boldsymbol{J}_{\mathrm{n}} \boldsymbol{\omega}_{\mathrm{n}} + \frac{1}{2} \boldsymbol{\omega}_{\mathrm{g}}^{\mathrm{T}} \boldsymbol{J}_{\mathrm{g}} \boldsymbol{\omega}_{\mathrm{g}} + \frac{1}{2} m_{\mathrm{h}} \boldsymbol{v}_{\mathrm{h}}^{\mathrm{T}} \boldsymbol{v}_{\mathrm{h}} + \\ &\frac{1}{2} \boldsymbol{\omega}_{\mathrm{h}}^{\mathrm{T}} \boldsymbol{J}_{\mathrm{h}} \boldsymbol{\omega}_{\mathrm{h}} + \frac{1}{2} \sum_{j=1}^{3} \int_0^{r_{\mathrm{b}}} \mu_{\mathrm{b}}(r) \boldsymbol{v}_{\mathrm{b}j}^{\mathrm{T}} \boldsymbol{v}_{\mathrm{b}j} \mathrm{d}r \end{aligned} \tag{4}$$

where $m_{\mathrm{p}}, m_{\mathrm{n}}, m_{\mathrm{h}}$ are the mass of the platform, nacelle, and hub, respectively. $\mu_{\mathrm{t}}(h), \mu_{\mathrm{b}}(r)$ are the distributed mass of the tower and blade. $\boldsymbol{J}_{\mathrm{p}}, \boldsymbol{J}_{\mathrm{n}}, \boldsymbol{J}_{\mathrm{g}}, \boldsymbol{J}_{\mathrm{h}}$ are the moment of inertia of the platform, nacelle, generator, and hub, respectively. $\boldsymbol{\omega}_{\mathrm{p}}, \boldsymbol{\omega}_{\mathrm{n}}, \boldsymbol{\omega}_{\mathrm{g}}, \boldsymbol{\omega}_{\mathrm{h}}$ are the angular velocity vector of the platform, nacelle, generator, and hub, respectively. $\boldsymbol{v}_{\mathrm{p}}, \boldsymbol{v}_{\mathrm{t}}, \boldsymbol{v}_{\mathrm{n}}, \boldsymbol{v}_{\mathrm{h}}, \boldsymbol{v}_{\mathrm{b}j}$ denotes the velocity vector of platform, tower, nacelle, hub and blade, as the time derivatives of the response vector $\boldsymbol{r}(t)$ (Mirtich, 1996).

The position vector of the platform in the global coordinate centroid $\boldsymbol{r}_{\mathrm{p}}(t)$ is defined as:

$$\boldsymbol{r}_{\mathrm{p}}(t) = \begin{Bmatrix} q_1 & q_2 & q_3 \end{Bmatrix}^{\mathrm{T}} + \boldsymbol{R}_{\mathrm{p}}^{\mathrm{T}} \begin{Bmatrix} 0 & 0 & h_{\mathrm{p}} \end{Bmatrix}^{\mathrm{T}} \tag{5}$$

where $\boldsymbol{R}_{\mathrm{p}}$ is the coordinate rotation matrix corresponding to the platform rotational angle $\{q_4, q_5, q_6\}$, from inertial reference frame $\boldsymbol{z}_1, \boldsymbol{z}_2, \boldsymbol{z}_3$ to platform frame $\boldsymbol{a}_1, \boldsymbol{a}_2, \boldsymbol{a}_3$. $(\ )^{\mathrm{T}}$ denotes transpose of the matrix. h_{p} is the vertical distance from the SWL to the mass center of platform. It is worth noting that, there exists a certain conversion relationship between the angular velocity $\boldsymbol{\omega}$ for the kinetic energy calculation and the Euler angular velocity $\boldsymbol{\theta}' = \{\theta_1', \theta_2', \theta_3'\}$, given by Fossen (2011):

$$\boldsymbol{\omega} = \boldsymbol{T}^{-1} \begin{Bmatrix} \theta_1' \\ \theta_2' \\ \theta_3' \end{Bmatrix} = \begin{bmatrix} 1 & 0 & s_{\theta_2'} \\ 0 & c_{\theta_1'} & -s_{\theta_1'} c_{\theta_2'} \\ 0 & s_{\theta_1'} & c_{\theta_1'} c_{\theta_2'} \end{bmatrix} \begin{Bmatrix} \theta_1' \\ \theta_2' \\ \theta_3' \end{Bmatrix} \tag{6}$$

where $\boldsymbol{T}^{-1}$ is the transformation matrix between Euler angular velocity vector and angular velocity vector. The angular velocity vector $\boldsymbol{\omega}_{\mathrm{p}}(t)$ of the platform is defined as:

$$\boldsymbol{\omega}_{\mathrm{p}}(t) = \boldsymbol{T}_{\mathrm{p}}^{-1} \begin{Bmatrix} q_4' & q_5' & q_6' \end{Bmatrix}^{\mathrm{T}} \tag{7}$$

where $\boldsymbol{T}_{\mathrm{p}}^{-1}$ is the transformation matrix between Euler angular velocity vector and angular velocity vector of platform $\{q_4, q_5, q_6\}$.

The position vector $\boldsymbol{r}_{\mathrm{t}}(h, t)$ of the tower in global coordinate is defined as:

$$\boldsymbol{r}_{\mathrm{t}}(h, t) = \begin{Bmatrix} q_1 \\ q_2 \\ q_3 \end{Bmatrix} + \boldsymbol{R}_{\mathrm{p}}^{\mathrm{T}} \left(\begin{Bmatrix} 0 \\ 0 \\ h_{\mathrm{b}} + h \end{Bmatrix} + \begin{Bmatrix} \phi_1^{\mathrm{TFA}}(h) q_7(t) \\ \phi_1^{\mathrm{TSS}}(h) q_8(t) \\ -v_{\mathrm{t}}(h, t) \end{Bmatrix} \right) \tag{8}$$

where h_{b} is the vertical distance of SWL to tower-base. $\phi_1^{\mathrm{TFA}}(h), \phi_1^{\mathrm{TSS}}(h)$ denote the tower fore-aft and side-side fundamental mode shapes, respectively. $v_{\mathrm{t}}(h, t)$is the axial deflection of the tower. The axial deflection was attributed to assuming that the flexible beam remains fixed in length (Jonkman, 2003) instead of the compression of the tower, given by:

$$v_{\mathrm{t}}(h, t) = \frac{1}{2} \left(S_{\mathrm{TFA}} q_7^2 + S_{\mathrm{TSS}} q_8^2 \right) \tag{9}$$

$$S_{\mathrm{TFA}} = \int_0^h \left(\frac{\mathrm{d}\phi_1^{\mathrm{TFA}}}{\mathrm{d}h_1} \right)^2 \mathrm{d}h_1, S_{\mathrm{TSS}} = \int_0^h \left(\frac{\mathrm{d}\phi_1^{\mathrm{TSS}}}{\mathrm{d}h_1} \right)^2 \mathrm{d}h_1 \tag{10}$$

The position vector $\boldsymbol{r}_{\mathrm{n}}(t)$ of the nacelle in global coordinate can be determined as:

$$\boldsymbol{r}_{\mathrm{n}}(t) = \begin{Bmatrix} q_1 \\ q_2 \\ q_3 \end{Bmatrix} + \boldsymbol{R}_{\mathrm{p}}^{\mathrm{T}} \left(\begin{Bmatrix} q_7 \\ q_8 \\ h_{\mathrm{b}} + h_{\mathrm{t}} - v_{\mathrm{t}}(h_{\mathrm{t}}, t) \end{Bmatrix} + \boldsymbol{R}_{\mathrm{t}}^{\mathrm{T}} \begin{Bmatrix} d_{\mathrm{n}} \\ 0 \\ h_{\mathrm{n}} \end{Bmatrix} \right) \tag{11}$$

$$\theta_{\mathrm{SS}} = -\left. \frac{\mathrm{d}\phi_1^{\mathrm{TSS}}}{\mathrm{d}h} \right|_{h = h_{\mathrm{t}}} q_7, \theta_{\mathrm{FA}} = \left. \frac{\mathrm{d}\phi_1^{\mathrm{TFA}}}{\mathrm{d}h} \right|_{h = h_{\mathrm{t}}} q_8 \tag{12}$$

where $d_{\mathrm{n}}, h_{\mathrm{n}}$ are downwind and vertical distance from the tower-top to the mass center of nacelle, respectively. $\boldsymbol{R}_{\mathrm{t}}$ is the coordinate rotation matrix corresponding to the tower rotational angle $\{\theta_{\mathrm{SS}}, \theta_{\mathrm{FA}}, 0\}$, from tower-base frame $\boldsymbol{a}_1, \boldsymbol{a}_2, \boldsymbol{a}_3$ to nacelle frame $\boldsymbol{d}_1, \boldsymbol{d}_2, \boldsymbol{d}_3$. $\theta_{\mathrm{SS}}, \theta_{\mathrm{FA}}$ are the additional rotation of the tower when the tower vibrates longitudinally and transversely. h_{t} is the height of the tower.

The angular velocity vector $\boldsymbol{\omega}_{\mathrm{n}}(t)$ of the nacelle is defined as:

$$\boldsymbol{\omega}_{\mathrm{n}}(t) = \boldsymbol{T}_{\mathrm{p}}^{-1} \begin{Bmatrix} q_4' \\ q_5' \\ q_6' \end{Bmatrix} + \boldsymbol{R}_{\mathrm{p}}^{\mathrm{T}} \boldsymbol{T}_{\mathrm{t}}^{-1} \begin{Bmatrix} \theta_{\mathrm{SS}}' \\ \theta_{\mathrm{FA}}' \\ 0 \end{Bmatrix} \tag{13}$$

where $\boldsymbol{T}_{\mathrm{p}}^{-1}$ is the transformation matrix between Euler angular velocity vector and angular velocity vector of tower $\{\theta_{\mathrm{SS}}, \theta_{\mathrm{FA}}, 0\}$.

The angular velocity vector $\boldsymbol{\omega}_{\mathrm{g}}(t)$ of the generator is defined as:

$$\boldsymbol{\omega}_{\mathrm{g}} = \boldsymbol{T}_{\mathrm{p}}^{-1}\begin{Bmatrix} q_4' \\ q_5' \\ q_6' \end{Bmatrix} + \boldsymbol{R}_{\mathrm{p}}^{\mathrm{T}}\boldsymbol{T}_{\mathrm{t}}^{-1}\begin{Bmatrix} \theta_{\mathrm{SS}}' \\ \theta_{\mathrm{FA}}' \\ 0 \end{Bmatrix} + \boldsymbol{R}_{\mathrm{p}}^{\mathrm{T}}\boldsymbol{R}_{\mathrm{t}}^{\mathrm{T}}\boldsymbol{R}_{\mathrm{s}}^{\mathrm{T}}\begin{Bmatrix} N_{\mathrm{Gear}} \cdot q_{10}' \\ 0 \\ 0 \end{Bmatrix} \quad (14)$$

where $\boldsymbol{R}_{\mathrm{s}}$ is the coordinate rotation matrix corresponding to the rotor shaft tilt angle $\{0, \theta_{\mathrm{s}}, 0\}$, from nacelle frame $\boldsymbol{d}_1, \boldsymbol{d}_2, \boldsymbol{d}_3$ to shaft frame $\boldsymbol{c}_1, \boldsymbol{c}_2, \boldsymbol{c}_3$. θ_{s} is rotor shaft tilt angle. N_{Gear} is gearbox ratio from high-speed to low-speed.

The position vector $\boldsymbol{r}_{\mathrm{h}}(t)$ of the hub in global coordinate is defined as:

$$\boldsymbol{r}_{\mathrm{h}}(t) = \begin{Bmatrix} q_1 \\ q_2 \\ q_3 \end{Bmatrix} + \boldsymbol{R}_{\mathrm{p}}^{\mathrm{T}}\left[\begin{Bmatrix} q_7 \\ q_8 \\ h_{\mathrm{b}} + h_{\mathrm{t}} - v_{\mathrm{t}}(h_{\mathrm{t}}, t) \end{Bmatrix} + \boldsymbol{R}_{\mathrm{t}}^{\mathrm{T}}\left(\begin{bmatrix} 0 \\ 0 \\ h_{\mathrm{s}} \end{bmatrix} + \boldsymbol{R}_{\mathrm{s}}^{\mathrm{T}}\begin{bmatrix} d_{\mathrm{h}} \\ 0 \\ 0 \end{bmatrix}\right)\right] \quad (15)$$

where h_{s} is the vertical distance from the tower-top to the rotor shaft. d_{h} is the distance from $\boldsymbol{c}_3$ axis to hub centroid.

The angular velocity vector $\boldsymbol{\omega}_{\mathrm{h}}(t)$ of the hub can be determined as:

$$\boldsymbol{\omega}_{\mathrm{h}}(t) = \boldsymbol{T}_{\mathrm{p}}^{-1}\begin{Bmatrix} q_4' \\ q_5' \\ q_6' \end{Bmatrix} + \boldsymbol{R}_{\mathrm{p}}^{\mathrm{T}}\boldsymbol{T}_{\mathrm{t}}^{-1}\begin{Bmatrix} \theta_{\mathrm{SS}}' \\ \theta_{\mathrm{FA}}' \\ 0 \end{Bmatrix} + \boldsymbol{R}_{\mathrm{p}}^{\mathrm{T}}\boldsymbol{R}_{\mathrm{t}}^{\mathrm{T}}\boldsymbol{R}_{\mathrm{s}}^{\mathrm{T}}\begin{Bmatrix} q_9' + q_{10}' \\ 0 \\ 0 \end{Bmatrix} \quad (16)$$

The position vector $\boldsymbol{r}_{\mathrm{bj}}(r, t)$ of the cross-section with a distance r from center of rotation for j^{th} blade in global coordinate is defined as:

$$\begin{aligned} \boldsymbol{r}_{\mathrm{bj}}(r, t) = &\begin{Bmatrix} q_1 \\ q_2 \\ q_3 \end{Bmatrix} + \boldsymbol{R}_{\mathrm{p}}^{\mathrm{T}}\begin{Bmatrix} q_7 \\ q_8 \\ h_{\mathrm{b}} + h_{\mathrm{t}} - v_{\mathrm{t}}(h_{\mathrm{t}}, t) \end{Bmatrix} + \\ &\boldsymbol{R}_{\mathrm{p}}^{\mathrm{T}}\boldsymbol{R}_{\mathrm{t}}^{\mathrm{T}}\begin{Bmatrix} 0 \\ 0 \\ h_{\mathrm{s}} \end{Bmatrix} + \boldsymbol{R}_{\mathrm{p}}^{\mathrm{T}}\boldsymbol{R}_{\mathrm{t}}^{\mathrm{T}}\boldsymbol{R}_{\mathrm{s}}^{\mathrm{T}}\begin{Bmatrix} d_{\mathrm{h}} \\ 0 \\ 0 \end{Bmatrix} + \\ &\boldsymbol{R}_{\mathrm{p}}^{\mathrm{T}}\boldsymbol{R}_{\mathrm{t}}^{\mathrm{T}}\boldsymbol{R}_{\mathrm{s}}^{\mathrm{T}}\boldsymbol{R}_{\mathrm{aj}}^{\mathrm{T}}\boldsymbol{R}_{\mathrm{c}}^{\mathrm{T}}\boldsymbol{R}_{\mathrm{bj}}^{\mathrm{T}}\begin{Bmatrix} \phi_{\mathrm{BF}}(r)q_{10+j} + \phi_{\mathrm{BE}}(r)q_{13+j} \\ \psi_{\mathrm{BF}}(r)q_{10+j} + \psi_{\mathrm{BE}}(r)q_{13+j} \\ r_{\mathrm{hub}} + r - v_{\mathrm{bj}}(r, t) \end{Bmatrix} \end{aligned} \quad (17)$$

where $\boldsymbol{R}_{\mathrm{aj}}^{\mathrm{T}}, \boldsymbol{R}_{\mathrm{c}}^{\mathrm{T}}, \boldsymbol{R}_{\mathrm{bj}}^{\mathrm{T}}$ are the coordinate rotation matrix corresponding to the azimuth angle $\{\psi_j, 0, 0\}$, blade cone angle $\{0, \theta_{\mathrm{c}}, 0\}$, and blade pitch angle $\{0, 0, \theta_{\mathrm{p}}\}$, from shaft frame $\boldsymbol{c}_1, \boldsymbol{c}_2, \boldsymbol{c}_3$ to hub frame $\boldsymbol{g}'^{j}_1, \boldsymbol{g}'^{j}_2, \boldsymbol{g}'^{j}_3$, hub frame $\boldsymbol{g}'^{j}_1, \boldsymbol{g}'^{j}_2, \boldsymbol{g}'^{j}_3$ to blade cone frame $\boldsymbol{i}_1^j, \boldsymbol{i}_2^j, \boldsymbol{i}_3^j$, and blade cone frame $\boldsymbol{i}_1^j, \boldsymbol{i}_2^j, \boldsymbol{i}_3^j$ to blade frame $\boldsymbol{j}_1^j, \boldsymbol{j}_2^j, \boldsymbol{j}_3^j$ respectively. r_{hub} is hub radius. $\phi_{\mathrm{BF}}(r), \phi_{\mathrm{BE}}(r)$ are the mode shapes of blade out-of-plane and $\psi_{\mathrm{BF}}(r), \psi_{\mathrm{BE}}(r)$ are the mode shapes of blade in-plane (Jonkman, 2003), and they are given by the following expressions:

$$\phi_{\mathrm{BF}}(r) = \int_0^r \left\{ \int_0^{r_1} \frac{\mathrm{d}^2\varphi_{\mathrm{BF}}(r_2)}{\mathrm{d}r_2^2} \cos\left[\theta_{\mathrm{b}}(r_2)\right] \mathrm{d}r_2 \right\} \mathrm{d}r_1 \quad (18)$$

$$\phi_{\mathrm{BE}}(r) = \int_0^r \left\{ \int_0^{r_1} \frac{\mathrm{d}^2\varphi_{\mathrm{BE}}(r_2)}{\mathrm{d}r_2^2} \sin\left[\theta_{\mathrm{b}}(r_2)\right] \mathrm{d}r_2 \right\} \mathrm{d}r_1 \quad (19)$$

$$\psi_{\mathrm{BF}}(r) = -\int_0^r \left\{ \int_0^{r_1} \frac{\mathrm{d}^2\varphi_{\mathrm{BF}}(r_2)}{\mathrm{d}r_2^2} \sin\left[\theta_{\mathrm{b}}(r_2)\right] \mathrm{d}r_2 \right\} \mathrm{d}r_1 \quad (20)$$

$$\psi_{\mathrm{BE}}(r) = \int_0^r \left\{ \int_0^{r_1} \frac{\mathrm{d}^2\varphi_{\mathrm{BE}}(r_2)}{\mathrm{d}r_2^2} \cos\left[\theta_{\mathrm{b}}(r_2)\right] \mathrm{d}r_2 \right\} \mathrm{d}r_1 \quad (21)$$

where $\varphi_{\mathrm{BF}}(r), \varphi_{\mathrm{BE}}(r)$ are the flapwise and edgewise blade mode shapes. $\theta_{\mathrm{b}}(r)$ is the blade twist angle as:

$$\theta_{\mathrm{b}}(r) = \theta + \theta_{\mathrm{p}} \quad (22)$$

where θ is blade structural pre-twist angle. In addition, $v_{\mathrm{bj}}(r, t)$ is the axial deflection of the blade j, which is the same as the axial deflection of tower, given by:

$$v_{\mathrm{bj}} = \frac{1}{2}\left(S_{\mathrm{BF}}q_{10+j}^2 + S_{\mathrm{BE}}q_{13+j}^2 + S_{\mathrm{BFE}}q_{10+j}q_{13+j}\right) \quad (23)$$

$$\begin{cases} S_{\mathrm{BF}} = \int_0^r \left[\left(\frac{\mathrm{d}\phi_{\mathrm{BF}}}{\mathrm{d}r_1}\right)^2 + \left(\frac{\mathrm{d}\psi_{\mathrm{BF}}}{\mathrm{d}r_1}\right)^2\right] \mathrm{d}r_1 \\ S_{\mathrm{BE}} = \int_0^r \left[\left(\frac{\mathrm{d}\phi_{\mathrm{BE}}}{\mathrm{d}r_1}\right)^2 + \left(\frac{\mathrm{d}\psi_{\mathrm{BE}}}{\mathrm{d}r_1}\right)^2\right] \mathrm{d}r_1 \\ S_{\mathrm{BFE}} = \int_0^r \left(\frac{\mathrm{d}\phi_{\mathrm{BF}}}{\mathrm{d}r_1}\frac{\mathrm{d}\phi_{\mathrm{BE}}}{\mathrm{d}r_1} + \frac{\mathrm{d}\psi_{\mathrm{BF}}}{\mathrm{d}r_1}\frac{\mathrm{d}\psi_{\mathrm{BE}}}{\mathrm{d}r_1}\right) \mathrm{d}r_1 \end{cases} \quad (24)$$

The potential energy consisting of strain potential energy V_{beam} and gravity potential energy V_{Gravity} is defined as:

$$\begin{aligned} V_{\mathrm{beam}} = &\frac{1}{2}\int_0^{h_{\mathrm{t}}} \left[EI_{\mathrm{TFA}}\left(\frac{\mathrm{d}^2\phi_1^{\mathrm{TFA}}}{\mathrm{d}h^2}\right)^2 q_7^2 + EI_{\mathrm{TSS}}\left(\frac{\mathrm{d}^2\phi_1^{\mathrm{TSS}}}{\mathrm{d}h^2}\right)^2 q_8^2\right] \mathrm{d}h + \\ &\frac{1}{2}\sum_{j=0}^{2}\int_0^{r_{\mathrm{b}}} \left[EI_{\mathrm{BF}}\left(\frac{\mathrm{d}^2\varphi_{\mathrm{BF}}}{\mathrm{d}r^2}\right)^2 q_{11+j}^2 + EI_{\mathrm{BE}}\left(\frac{\mathrm{d}^2\varphi_{\mathrm{BE}}}{\mathrm{d}r^2}\right)^2 q_{14+j}^2\right] \mathrm{d}r + \\ &\frac{1}{2}k_{\mathrm{Dr}}q_9^2 \end{aligned} \quad (25)$$

$$V_{\text{Gravity}} = g\left(m_{\text{p}}\boldsymbol{r}_{\text{p}} + \int_0^{h_{\text{t}}}\mu_{\text{t}}(h)\boldsymbol{r}_{\text{t}}(h)\text{d}h + m_{\text{n}}\boldsymbol{r}_{\text{n}} + m_{\text{h}}\boldsymbol{r}_{\text{h}} + \sum_{j=1}^{3}\int_0^{r_{\text{b}}}\mu_{\text{b}}(r)\boldsymbol{r}_{\text{b}j}(r)\text{d}r\right)\cdot(0 \quad 0 \quad 1)^{\text{T}} \tag{26}$$

where $EI_{\text{TFA}}(h), EI_{\text{TSS}}(h)$ are the longitudinal and transverse distributed stiffnesses of the tower. $EI_{\text{BF}}(r), EI_{\text{BE}}(r)$ are the flapwise and edgewise distributed stiffnesses of the blade. r_{b} is the rotor radius of the FOWT. k_{Dr} is the equivalent stiffness of drivetrain.

Longitudinal and transverse damping (c_{TFA} and c_{TSS}) of tower, and the blade damping (c_{BF} and c_{BE}) along out-of-plane and in-plane are defined as:

$$c_{\text{TFA}} = 2\zeta_{\text{t}}\cdot\sqrt{\int_0^{h_{\text{t}}}\mu_{\text{t}}\phi_1^{\text{TFA}}\text{d}h}\cdot\sqrt{\int_0^{h_{\text{t}}}EI_{\text{TFA}}\left(\frac{\text{d}^2\phi_1^{\text{TFA}}}{\text{d}h^2}\right)^2\text{d}h} \tag{27}$$

$$c_{\text{TSS}} = 2\zeta_{\text{t}}\cdot\sqrt{\int_0^{h_{\text{t}}}\mu_{\text{t}}\phi_1^{\text{TSS}}\text{d}h}\cdot\sqrt{\int_0^{h_{\text{t}}}EI_{\text{TSS}}\left(\frac{\text{d}^2\phi_1^{\text{TSS}}}{\text{d}h^2}\right)^2\text{d}h} \tag{28}$$

$$c_{\text{BF}} = 2\zeta_{\text{b}}\cdot\sqrt{\int_0^{r_{\text{b}}}\mu_{\text{b}}\varphi_{\text{BF}}^2\text{d}r}\cdot\sqrt{\int_0^{r_{\text{b}}}EI_{\text{BF}}\left(\frac{\text{d}^2\varphi_{\text{BF}}}{\text{d}r^2}\right)^2\text{d}r} \tag{29}$$

$$c_{\text{BE}} = 2\zeta_{\text{b}}\cdot\sqrt{\int_0^{r_{\text{b}}}\mu_{\text{b}}\varphi_{\text{BE}}^2\text{d}r}\cdot\sqrt{\int_0^{r_{\text{b}}}EI_{\text{BE}}\left(\frac{\text{d}^2\varphi_{\text{BE}}}{\text{d}r^2}\right)^2\text{d}r} \tag{30}$$

where ζ_{t} and ζ_{b} denote damping ratio of tower and blade, respectively.

2.3 Wind turbine control system

A conventional variable-speed and variable blade-pitch control system is used in this study, which relies on the design of two basic control systems: the generator-torque controller and the full-span rotor-collective blade-pitch controller.

2.3.1 Variable-speed control

As illustrated in Figure 3, the generator-torque controller incorporates five control regions (Larsen and Hanson, 2007). The relationship between generator torque T_{g} and generator speed Ω can be expressed as:

$$T_{\text{g}} = \begin{cases} 0 & \Omega \leqslant 670\ \text{r/min} \\ 96.533\,8(\Omega - 670) & 670\ \text{r/min} < \Omega \leqslant 871\ \text{r/min} \\ 0.025\,576\,4\Omega^2 & 871\ \text{r/min} < \Omega \leqslant 1\,137.442\ \text{r/min} \\ 407.955\,4(\Omega - 1\,056.33) & 1\,137.442\ \text{r/min} < \Omega \leqslant 1\,161.963\ \text{r/min} \\ 43\,093.55 & \Omega > 1\,161.963\ \text{r/min} \end{cases} \tag{31}$$

Further, the generator load can be defined as:

$$F_i^{\text{g}} = \begin{cases} -N_{\text{Gear}}T_{\text{g}} & i = 10 \\ 0 & \text{else} \end{cases} \tag{32}$$

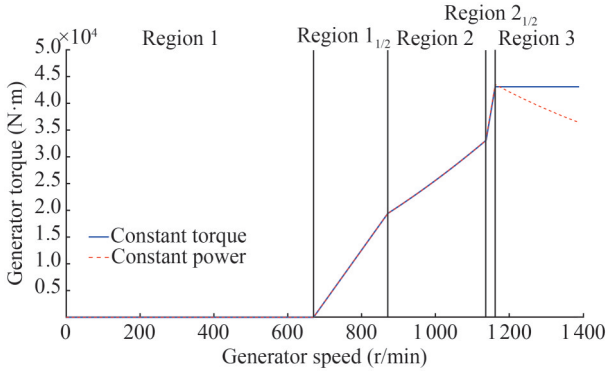


Figure 3 Torque-versus-speed response of the variable-speed controller (Larsen and Hanson, 2007)

2.3.2 Blade-pitch control

The proportional-integral (PI) control on the speed error between the generator speed and the rated generator speed is used to determine the blade pitch angle, given by:

$$\Delta\theta_{\text{p}} = K_{\text{P}}N_{\text{Gear}}\Delta\Omega + K_{\text{I}}\int_0^t N_{\text{Gear}}\Delta\Omega\text{d}t + K_{\text{D}}N_{\text{Gear}}\Delta\Omega' \tag{33}$$

where $\Delta\theta_{\text{p}}$ is variation value of blade pitch angle. $\Delta\Omega$ is the variation between the low-speed shaft speed and the rated speed. $\Delta\Omega'$ is the low-speed shaft rotational acceleration. $K_{\text{P}}, K_{\text{I}}, K_{\text{D}}$ are the blade-pitch controller proportional, integral, and derivative gains, respectively. In order to avoid negative damping caused by controller, the derivative gain K_{D} is neglected. Whereas, proportional and integral gain $K_{\text{P}}, K_{\text{I}}$ can be simplified by the linear relation between pitch sensitivity and blade-pitch angle defined as:

$$K_{\text{P}}(\theta_{\text{p}}) = \frac{2I_{\text{Drivetrain}}\Omega_0\zeta_\varphi\omega_{\varphi n}}{N_{\text{Gear}}\left[-\dfrac{\partial P}{\partial\theta_{\text{p}}}(\theta_{\text{p}} = 0)\right]}GK(\theta_{\text{p}}) \tag{34}$$

$$K_{\text{I}}(\theta_{\text{p}}) = \frac{I_{\text{Drivetrain}}\Omega_0\omega_{\varphi n}^2}{N_{\text{Gear}}\left[-\dfrac{\partial P}{\partial\theta_{\text{p}}}(\theta_{\text{p}} = 0)\right]}GK(\theta_{\text{p}}) \tag{35}$$

$$GK(\theta_{\text{p}}) = \frac{1}{1 + \theta_{\text{p}}/\theta_{\text{K}}} \tag{36}$$

where θ_p is blade pitch angle. $I_{\text{Drivetrain}}$ is the drivetrain inertia cast to the low-speed shaft. Ω_0 is the rated low-speed shaft rotational speed, given by $\Omega_0 = 122.909\,6$ rad/s. $GK\left(\theta_p\right)$ is the dimensionless gain-correction factor. θ_K is the blade-pitch angle at which the pitch sensitivity has doubled from its value at the rated operating point, given by $\theta_K = 6.302\,336°$. $\omega_{\varphi n}$, ζ_φ are the natural frequency and damping ratio of controller, given by $\omega_{\varphi n} = 0.21$ rad/s and $\zeta_\varphi = 0.7$, to avoid the negative damping of the platform-pitch mode (Larsen and Hanson, 2007).

3 Loadings

3.1 Aerodynamic load

Herein, the wind speed time history here is generated by TurbSim software (Jonkman and Kilcher, 2012). It is noted that the three-dimensional wind field from TurbSim is only related to y, z, t. Whereas the wind speed can be extended to be related to x, y, z, t by Taylor's frozen turbulence hypothesis (Higgins et al., 2012), which can be expressed as follows:

$$V\left(y,z,t\right) = V\left(y,z,t+\frac{x}{V_m}\right) \tag{37}$$

where V_m is the average wind speed at hub height.

The aerodynamic load is calculated by the blade element momentum theory corrected by Prandtl's hub/tip loss and Glauert's turbulent wake state with Buhl's modification (Ning et al., 2015). As shown in Figure 4, φ is local inflow angle. $V_{\text{rel},x}$, $V_{\text{rel},y}$, V_{rel} is the relative velocity of the inflow wind and the blade. a, a' denote axial and tangential induction factor, respectively. α is angle of attack. p_L, p_D denote blade lift and drag, respectively. p_x, p_y denote normal and tangential loads, respectively. Note that the positive direction for p_y is opposite to the y axis. From Figure 4, it can be seen that

$$\tan\varphi = \frac{V_{\text{rel},x}\left(1-a\right)}{V_{\text{rel},y}\left(1+a'\right)} \tag{38}$$

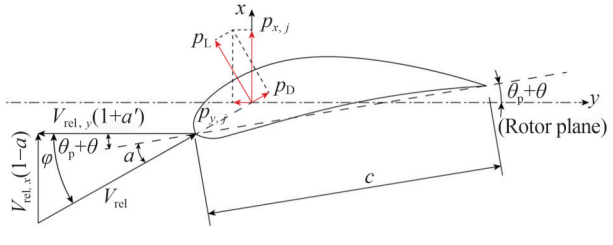


Figure 4 Blade element section subjected to local velocity and aerodynamic loading

$$a = \begin{cases} \kappa/\left(1+\kappa\right) & \varphi > 0, \kappa \leqslant 2/3 \\ \left(\gamma_1 - \sqrt{\gamma_2}\right)/\gamma_3 & \varphi > 0, \kappa > 2/3 \\ 1 - 1/2\sqrt{\gamma_2} & \gamma_3 = 0 \\ \kappa/\left(1+\kappa\right) & \varphi < 0, \kappa > 1 \\ 0 & \varphi < 0, \kappa \leqslant 1 \end{cases} \tag{39}$$

$$a' = \frac{\kappa'}{1-\kappa'} \tag{40}$$

$$\kappa = \frac{\sigma C_x}{4F\sin^2\varphi}, \kappa' = \frac{\sigma C_y}{4F\sin\varphi\cos\varphi} \tag{41}$$

$$F = F_{\text{tip}} \cdot F_{\text{hub}} = \frac{2}{\pi}\cos^{-1}\left(e^{-\frac{B}{2}\frac{r_b - r}{r\sin\varphi}}\right) \cdot \frac{2}{\pi}\cos^{-1}\left(e^{-\frac{B}{2}\frac{r - r_{\text{hub}}}{r_{\text{hub}}\sin\varphi}}\right) \tag{42}$$

$$\begin{cases} \gamma_1 = 2F\kappa - \left(\dfrac{10}{9} - F\right) \\ \gamma_2 = 2F\kappa - F\left(\dfrac{4}{3} - F\right) \\ \gamma_3 = 2F\kappa - \left(\dfrac{25}{9} - 2F\right) \end{cases} \tag{43}$$

where κ, κ' are relevant nondimensional parameters. r is local radial position. B is the number of blades. c is blade chord. F is a hub/tip loss correction.

The normal load p_y and tangential load p_x are determined as:

$$p_x = \frac{1}{2}\rho_a V_{\text{rel}}^2 c\left(C_l\cos\varphi + C_d\sin\varphi\right) \tag{44}$$

$$p_y = \frac{1}{2}\rho_a V_{\text{rel}}^2 c\left(C_l\sin\varphi - C_d\cos\varphi\right) \tag{45}$$

where C_l, C_d denote lift and drag coefficient, respectively. ρ_a is the density of air.

After the normal force and tangential force are obtained by the blade element momentum theory, the blade aerodynamic load in the blade aerodynamic coordinate system can be transformed to the inertial coordinate system, given by

$$\boldsymbol{f}_{a,j} = \boldsymbol{R}_p^T\boldsymbol{R}_t^T\boldsymbol{R}_s^T\boldsymbol{R}_{aj}^T\boldsymbol{R}_c^T\boldsymbol{R}_{bt}^T\boldsymbol{R}_{brj}^T\boldsymbol{R}_{bt}\begin{Bmatrix} p_{x,j} \\ -p_{y,j} \\ 0 \end{Bmatrix} \tag{46}$$

where $\boldsymbol{R}_{bt}, \boldsymbol{R}_{brj}$ are the transformation matrix corresponding to the blade twist angle $\left\{0, 0, \theta + \theta_p\right\}$ and blade rotation angle along normal and tangential direction $\left\{\theta_{Bjx}, \theta_{Bjy}, 0\right\}$ as:

$$\begin{cases} \theta_{Bjx} = \cos\theta \cdot \theta_{BjI} - \sin\theta \cdot \theta_{BjO} \\ \theta_{Bjy} = \sin\theta \cdot \theta_{BjI} + \cos\theta \cdot \theta_{BjO} \end{cases} \tag{47}$$

$$\begin{cases}\theta_{\mathrm{BjI}} = -\psi_{\mathrm{BF}}(r)q_{10+j} - \psi_{\mathrm{BE}}(r)q_{13+j} \\ \theta_{\mathrm{BjO}} = \phi_{\mathrm{BF}}(r)q_{10+j} + \phi_{\mathrm{BE}}(r)q_{13+j}\end{cases} \tag{48}$$

where θ_{BjI}, θ_{BjO} represent blade's additional angles caused by in-plane and out-plane deflection.

In summary, the generalized aerodynamic load can be represented as:

$$\boldsymbol{r}_{\mathrm{a,t}} = \begin{Bmatrix} q_7 \\ q_8 \\ h_{\mathrm{b}} + h_{\mathrm{t}} - v_{\mathrm{t}}(h_{\mathrm{t}}, t)\end{Bmatrix}, \boldsymbol{r}_{\mathrm{a,h}} = \begin{Bmatrix} 0 \\ 0 \\ h_{\mathrm{s}}\end{Bmatrix} + \boldsymbol{R}_{\mathrm{s}}^{\mathrm{T}}\begin{Bmatrix} d_{\mathrm{h}} \\ 0 \\ 0\end{Bmatrix}$$
$$\boldsymbol{r}_{\mathrm{a,b}j} = \begin{Bmatrix} u_{\mathrm{BjO}}(r,t) \\ u_{\mathrm{BjI}}(r,t) \\ r_{\mathrm{hub}} + r - v_{\mathrm{b}j}(r,t)\end{Bmatrix} \tag{50}$$

$$F_i^{\mathrm{a}} = \begin{cases} \sum_{j=1}^{3}\int_0^{r_{\mathrm{b}}} \boldsymbol{f}_{\mathrm{a},j}(i)\,\mathrm{d}r & i = 1,2,3 \\ \sum_{j=1}^{3}\int_0^{r_{\mathrm{b}}} \boldsymbol{f}_{\mathrm{a},j}^{\mathrm{T}}\left[\frac{\partial \boldsymbol{R}_{\mathrm{p}}^{\mathrm{T}}}{\partial q_i}\left(\boldsymbol{r}_{\mathrm{a,t}} + \boldsymbol{R}_{\mathrm{t}}^{\mathrm{T}}\boldsymbol{r}_{\mathrm{a,h}} + \boldsymbol{R}_{\mathrm{t}}^{\mathrm{T}}\boldsymbol{R}_{\mathrm{s}}^{\mathrm{T}}\boldsymbol{R}_{\mathrm{a}j}^{\mathrm{T}}\boldsymbol{R}_{\mathrm{c}}^{\mathrm{T}}\boldsymbol{R}_{\mathrm{b}j}^{\mathrm{T}}\boldsymbol{r}_{\mathrm{a,b}j}\right)\right]\mathrm{d}r & i = 4,5,6 \\ \sum_{j=1}^{3}\int_0^{r_{\mathrm{b}}} \boldsymbol{f}_{\mathrm{a},j}^{\mathrm{T}}\left\{\boldsymbol{R}_{\mathrm{p}}^{\mathrm{T}}\left[\begin{Bmatrix} 1 \\ 0 \\ -S_{\mathrm{TFA}}q_7\end{Bmatrix} + \frac{\partial \boldsymbol{R}_{\mathrm{t}}^{\mathrm{T}}}{\partial q_7}\left(\boldsymbol{r}_{\mathrm{a,h}} + \boldsymbol{R}_{\mathrm{t}}^{\mathrm{T}}\boldsymbol{R}_{\mathrm{s}}^{\mathrm{T}}\boldsymbol{R}_{\mathrm{a}j}^{\mathrm{T}}\boldsymbol{R}_{\mathrm{c}}^{\mathrm{T}}\boldsymbol{R}_{\mathrm{b}j}^{\mathrm{T}}\boldsymbol{r}_{\mathrm{a,b}j}\right)\right]\right\}\mathrm{d}r & i = 7 \\ \sum_{j=1}^{3}\int_0^{r_{\mathrm{b}}} \boldsymbol{f}_{\mathrm{a},j}^{\mathrm{T}}\left\{\boldsymbol{R}_{\mathrm{p}}^{\mathrm{T}}\left[\begin{Bmatrix} 0 \\ 1 \\ -S_{\mathrm{TSS}}q_8\end{Bmatrix} + \frac{\partial \boldsymbol{R}_{\mathrm{t}}^{\mathrm{T}}}{\partial q_8}\left(\boldsymbol{r}_{\mathrm{a,h}} + \boldsymbol{R}_{\mathrm{t}}^{\mathrm{T}}\boldsymbol{R}_{\mathrm{s}}^{\mathrm{T}}\boldsymbol{R}_{\mathrm{a}j}^{\mathrm{T}}\boldsymbol{R}_{\mathrm{c}}^{\mathrm{T}}\boldsymbol{R}_{\mathrm{b}j}^{\mathrm{T}}\boldsymbol{r}_{\mathrm{a,b}j}\right)\right]\right\}\mathrm{d}r & i = 8 \\ \sum_{j=1}^{3}\int_0^{r_{\mathrm{b}}} \boldsymbol{f}_{\mathrm{a},j}^{\mathrm{T}}\left(\boldsymbol{R}_{\mathrm{p}}^{\mathrm{T}}\boldsymbol{R}_{\mathrm{t}}^{\mathrm{T}}\boldsymbol{R}_{\mathrm{s}}^{\mathrm{T}}\frac{\partial \boldsymbol{R}_{\mathrm{a}j}^{\mathrm{T}}}{\partial q_i}\boldsymbol{R}_{\mathrm{c}}^{\mathrm{T}}\boldsymbol{R}_{\mathrm{b}j}^{\mathrm{T}}\boldsymbol{r}_{\mathrm{a,b}j}\right)\mathrm{d}r & i = 9,10 \\ \int_0^{r_{\mathrm{b}}} \boldsymbol{f}_{\mathrm{a},j}^{\mathrm{T}}\left(\boldsymbol{R}_{\mathrm{p}}^{\mathrm{T}}\boldsymbol{R}_{\mathrm{t}}^{\mathrm{T}}\boldsymbol{R}_{\mathrm{s}}^{\mathrm{T}}\boldsymbol{R}_{\mathrm{a}j}^{\mathrm{T}}\boldsymbol{R}_{\mathrm{c}}^{\mathrm{T}}\boldsymbol{R}_{\mathrm{b}j}^{\mathrm{T}}\begin{Bmatrix} \phi_{\mathrm{BF}} \\ \psi_{\mathrm{BF}} \\ -\left(S_{\mathrm{BF}}q_{10+j} + S_{\mathrm{BFE}}q_{13+j}\right)\end{Bmatrix}\right)\mathrm{d}r & i = 11,12,13 \\ \int_0^{r_{\mathrm{b}}} \boldsymbol{f}_{\mathrm{a},j}^{\mathrm{T}}\left(\boldsymbol{R}_{\mathrm{p}}^{\mathrm{T}}\boldsymbol{R}_{\mathrm{t}}^{\mathrm{T}}\boldsymbol{R}_{\mathrm{s}}^{\mathrm{T}}\boldsymbol{R}_{\mathrm{a}j}^{\mathrm{T}}\boldsymbol{R}_{\mathrm{c}}^{\mathrm{T}}\boldsymbol{R}_{\mathrm{b}j}^{\mathrm{T}}\begin{Bmatrix} \phi_{\mathrm{BE}} \\ \psi_{\mathrm{BE}} \\ -\left(S_{\mathrm{BE}}q_{13+j} + S_{\mathrm{BFE}}q_{10+j}\right)\end{Bmatrix}\right)\mathrm{d}r & i = 14,15,16 \end{cases} \tag{49}$$

3.2 Hydrostatic load

The total generalized load on the floating platform from linear hydrostatics F_i^{hs} can be denoted as follows:

$$F_i^{\mathrm{hs}} = \rho_{\mathrm{w}} g V_0 \delta_{i3} - \sum_{j=1}^{6} \boldsymbol{C}_{ij}^{\mathrm{hs}} q_j,\ i = 1,2,\cdots,6 \tag{51}$$

where ρ_{w} is the water density. g is the gravitational acceleration constant. V_0 is the displacement when the platform is at rest. δ_{ij} is the Kronecker-Delta function. $\boldsymbol{C}_{ij}^{\mathrm{hs}}$ is the linear hydrostatic-restoring matrix indicating the effects of waterplane area and the center of buoyancy (Jonkman, 2010).

3.3 Hydrodynamic load

The vertical load of the floating platform cannot be estimated by the Morison equation, which is commonly used to determine the hydrodynamic effect of fixed bottom support structures, due to its relatively small ratio of structural diameter to the wavelength. Therefore, Jonkman (2009) applied the linear potential-flow theory to calculate the hydrodynamic load, which combines the advantages of potential flow theory and the Morison equation. The total hydrodynamic load (F_i^{hd}) acting on the support platform can be obtained as follows:

$$F_i^{\mathrm{hd}} = \begin{cases} \sum_{j=1}^{6}\left(-\boldsymbol{A}_{ij}(\omega)q_j'' + F_i^{\mathrm{W}} + \int_{-h_{\mathrm{pb}}}^{0}\mathrm{d}F_i^{\mathrm{D}}\mathrm{d}z - \int_0^t \boldsymbol{K}_{ij}(t-\tau)q_j'(\tau)\mathrm{d}\tau\right) + B_{ij}q_j & i = 1,2 \\ \sum_{j=1}^{6}\left(-\boldsymbol{A}_{ij}(\omega)q_j'' + F_i^{\mathrm{W}} - \int_0^t \boldsymbol{K}_{ij}(t-\tau)q_j'(\tau)\mathrm{d}\tau\right) + B_{ij}q_j & i = 3 \\ \sum_{j=1}^{6}\left(-\boldsymbol{A}_{ij}(\omega)q_j'' + F_i^{\mathrm{W}} - \int_0^t \boldsymbol{K}_{ij}(t-\tau)q_j'(\tau)\mathrm{d}\tau + \int_{-h_{\mathrm{pb}}}^{0}\mathrm{d}\boldsymbol{F}^{\mathrm{D}}\frac{\partial \boldsymbol{R}_{\mathrm{p}}^{\mathrm{T}}}{\partial q_i}\begin{Bmatrix} 0 \\ 0 \\ z\end{Bmatrix}\mathrm{d}z\right) + B_{ij}q_j & i = 4,5,6 \\ 0 & \text{else} \end{cases} \tag{52}$$

$$F_i^{\mathrm{W}} = \sqrt{2}\sum_{n=0}^{N-1}\left(S_\zeta(\omega_n)\Delta\omega\right)^{1/2} X_i(\omega_n,\beta)\exp\left\{\mathrm{j}\left[\omega_n t + \phi_n - k(\omega_n)(x\cos\beta + y\sin\beta)\right]\right\} \tag{53}$$

$$\zeta(t,X,Y) = \sqrt{2}\sum_{n=0}^{N-1}\left(S_\zeta(\omega_n)\Delta\omega\right)^{1/2}\exp\left\{\mathrm{j}\left[\omega_n t + \phi_n - k(\omega_n)(x\cos\beta + y\sin\beta)\right]\right\} \tag{54}$$

$$\mathrm{d}F_i^{\mathrm{D}}(t,z) = \frac{1}{2}C_{\mathrm{D}}\rho_{\mathrm{w}}(D\mathrm{d}z)\left(v_{\mathrm{f},i} - v_{\mathrm{s},i}\right)\sqrt{\left(v_{\mathrm{f},1} - v_{\mathrm{s},1}\right)^2 + \left(v_{\mathrm{f},2} - v_{\mathrm{s},2}\right)^2},\ i = 1,2 \tag{55}$$

$$\mathrm{d}\boldsymbol{F}^{\mathrm{D}} = \left\{\mathrm{d}F_1^{\mathrm{D}} \quad \mathrm{d}F_2^{\mathrm{D}} \quad 0\right\} \tag{56}$$

where $\boldsymbol{A}_{ij}(\omega)$ is hydrodynamic-added-mass matrix. F_i^{W} represents the total excitation load on the support platform from incident waves. h_{pb} is the distance from the SWL to the bottom of platform. $\zeta(t)$ is wave elevation subjected to linear wave theory (Shinozuka and Deodatis, 1991). $S_\zeta(\omega_n)$ represents the desired one-sided power spectral density. ϕ_n is independent random phase angle distributed between $[0, 2\pi]$. $k(\omega)$ is the wave number. β is incident-wave propagation heading direction. $X_i(\omega_n,\beta)$ is normalized wave-excitation force. $\boldsymbol{K}_{ij}$ is the matrix of wave-radiation-retardation kernels. $\mathrm{d}F_i^{\mathrm{D}}$ is distributed viscous drag. C_{D} is drag coefficients in horizontal direction. D is the diameter of cylinder. $v_{\mathrm{f},i}$ and $v_{\mathrm{s},i}$ are the velocities of fluid and support platform, respectively. It is worth noting that an additional linear damping B_{ij} is introduced herein, since the Morison equation is not accurate enough to describe the hydrodynamic damping (Jonkman, 2010).

3.4 Mooring load

In this paper, the quasi-static method is adopted for the mooring load (Jonkman, 2009). Assuming that each cable is in static equilibrium at any time instant, the mooring tension can be obtained through the catenary equation. The method accounts for mooring nonlinearities and ignores the inertia and damping of the mooring system, which is suitable in various situations. If no portion of the line rests on the seabed ($L_{\mathrm{B}} = L - V_{\mathrm{F}}/\mu_{\mathrm{m}} \leqslant 0$), the analytical formulation is represented as follows:

$$x_{\mathrm{F}} = \frac{H_{\mathrm{F}}}{\mu_{\mathrm{m}}}\left\{\ln\left[\frac{V_{\mathrm{F}}}{H_{\mathrm{F}}} + \sqrt{1+\left(\frac{V_{\mathrm{F}}}{H_{\mathrm{F}}}\right)^2}\right] - \ln\left[\frac{V_{\mathrm{F}} - \mu_{\mathrm{m}}L}{H_{\mathrm{F}}} + \sqrt{1+\left(\frac{V_{\mathrm{F}} - \mu_{\mathrm{m}}L}{H_{\mathrm{F}}}\right)^2}\right]\right\} + \frac{H_{\mathrm{F}}L}{EA} \tag{57}$$

$$z_{\mathrm{F}} = \frac{H_{\mathrm{F}}}{\mu_{\mathrm{m}}}\left[\sqrt{1+\left(\frac{V_{\mathrm{F}}}{H_{\mathrm{F}}}\right)^2} - \sqrt{1+\left(\frac{V_{\mathrm{F}} - \mu_{\mathrm{m}}L}{H_{\mathrm{F}}}\right)^2}\right] + \frac{1}{EA}\left(V_{\mathrm{F}}L - \frac{\mu_{\mathrm{m}}L^2}{2}\right) \tag{58}$$

otherwise

$$x_{\mathrm{F}} = L - \frac{V_{\mathrm{F}}}{\mu_{\mathrm{m}}} + \frac{H_{\mathrm{F}}}{\mu_{\mathrm{m}}}\ln\left[\frac{V_{\mathrm{F}}}{H_{\mathrm{F}}} + \sqrt{1+\left(\frac{V_{\mathrm{F}}}{H_{\mathrm{F}}}\right)^2}\right] + \frac{H_{\mathrm{F}}L}{EA} + \frac{C_{\mathrm{B}}\mu_{\mathrm{m}}}{2EA}\times \left(\max\left(L - \frac{V_{\mathrm{F}}}{\mu_{\mathrm{m}}} - \frac{H_{\mathrm{F}}}{C_{\mathrm{B}}\mu_{\mathrm{m}}}, 0\right)\left(L - \frac{V_{\mathrm{F}}}{\mu_{\mathrm{m}}} - \frac{H_{\mathrm{F}}}{C_{\mathrm{B}}\mu_{\mathrm{m}}}\right) - \left(L - \frac{V_{\mathrm{F}}}{\mu_{\mathrm{m}}}\right)^2\right) \tag{59}$$

$$z_{\mathrm{F}} = \frac{H_{\mathrm{F}}}{\mu_{\mathrm{m}}}\left[\sqrt{1+\left(\frac{V_{\mathrm{F}}}{H_{\mathrm{F}}}\right)^2} - 1\right] + \frac{V_{\mathrm{F}}^2}{2EA\mu_{\mathrm{m}}} \tag{60}$$

where $(x_{\mathrm{F}}, z_{\mathrm{F}})$ is the fairlead position coordinates relative to the anchor. H_{F}, V_{F} is the horizontal and vertical tension of the fairlead, respectively. L is the unstretched length of a mooring line. μ_{m} is the apparent weight of a line in fluid per unit length of line as $\mu_{\mathrm{m}} = \left(\mu_{\mathrm{c}} - \rho_{\mathrm{w}}\pi D_{\mathrm{c}}^2/4\right)g$. μ_{c} is the mass of mooring line per unit length. D_{c} is the effective diameter of a mooring line. EA is the extensional stiffness of a mooring line. C_{B} is the coefficient of the static-friction drag between the seabed and a mooring line.

After obtaining the horizontal and vertical tension of the fairlead H_{F}, V_{F} from Eq.(57)–(60) by the Newton iteration method, the mooring tension ($\boldsymbol{f}_{\mathrm{m},j}$) on the fairlead can be determined by using coordinate transformation and Newton's third law

$$\boldsymbol{f}_{\mathrm{m},j} = -\left\{H_{\mathrm{F},j}\cos\beta_j \quad H_{\mathrm{F},j}\sin\beta_j \quad V_{\mathrm{F},j}\right\} \tag{61}$$

$$\beta_j = \arctan\left(\frac{y_{\mathrm{F},j} - y_{\mathrm{A},j}}{x_{\mathrm{F},j} - x_{\mathrm{A},j}}\right) \tag{62}$$

$$\boldsymbol{r}_{\mathrm{F},j} = \begin{Bmatrix} x_{\mathrm{F},j} \\ y_{\mathrm{F},j} \\ z_{\mathrm{F},j} \end{Bmatrix} = \begin{Bmatrix} q_1 \\ q_2 \\ q_3 \end{Bmatrix} + \boldsymbol{R}_{\mathrm{p}}^{\mathrm{T}}\begin{Bmatrix} x_{\mathrm{F},j}^{\mathrm{a}} \\ y_{\mathrm{F},j}^{\mathrm{a}} \\ z_{\mathrm{F},j}^{\mathrm{a}} \end{Bmatrix} \tag{63}$$

where j represents the number of moorings. β_j is the angle between the inertial coordinate system and the mooring coordinate system. $(x_{\mathrm{F},j}, y_{\mathrm{F},j}, z_{\mathrm{F},j})$ and $(x_{\mathrm{A},j}, y_{\mathrm{A},j}, z_{\mathrm{A},j})$ are the coordinates of the fairlead and anchor in the inertial coordinate system, respectively. $(x_{\mathrm{F},j}^{\mathrm{a}}, y_{\mathrm{F},j}^{\mathrm{a}}, z_{\mathrm{F},j}^{\mathrm{a}})$ are the coor-

dinates of the fairlead in the platform coordinate system.

In general, the generalized mooring load can be expressed as:

$$F_i^{\mathrm{m}} = \begin{cases} \sum_{j=1}^{3} \boldsymbol{f}_{\mathrm{m},j}(i) & i = 1, 2, 3 \\ \sum_{j=1}^{3} \boldsymbol{f}_{\mathrm{m},j} \dfrac{\partial \boldsymbol{R}_{\mathrm{p}}^{\mathrm{T}}}{\partial q_i} \boldsymbol{r}_{\mathrm{F},j} & i = 4, 5, 6 \\ 0 & \text{else} \end{cases} \tag{64}$$

4 Verification and calculation results analysis

In this section, the OC3-Hywind Spar floating platform equipped with a 5 MW wind turbine given by NREL in the report (Jonkman, 2010) is used as the benchmark to establish the coupled dynamic model, and the coupling dynamic equation is solved numerically by Runge-Kutta method. Its accuracy is verified by comparing with the results obtained by OpenFAST v3.0.0. The specific parameters of the platform and wind turbine are referred in the NREL report (Jonkman et al., 2009; Jonkman, 2010). At the same time, the responses of the FOWT model under the small-angle assumption and the non-small-angle assumption were compared to determine the impact of the small-angle assumption.

4.1 Dynamic characteristics

The coupled model is validated by comparing the natural frequency results with the numerical analysis using OpenFAST in Table 1. It can be found that the natural frequencies of the Spar FOWT can be accurately determined by the coupled model established in this paper.

4.2 Comparison of free vibration response

With the initial parameters $q_4, q_5, q_6 = 5°$, the responses of free vibrations of the proposed coupled model in the time domain are plotted in Figure 5. By comparing with the computational results, it can be seen that the responses of the coupled model are almost consistent with the results given by OpenFAST, except for the yaw. The yaw frequencies are 0.121 7 Hz and 0.103 3 Hz, respectively, with an error of 17.8%.

Figure 6 shows the single-sided amplitude spectrum of the platform yaw, with the parameter $q_4 = 5°$, $q_5 = 5°$ and $q_6 = 5°$, respectively. From Figure 6(a)–(b), under the conditions with $q_4 = 5°$ and $q_5 = 5°$, there exist obvious differences in the yaw of the platform between the results of the coupled model and OpenFAST. The corresponding yaw frequencies are 0.121 7 Hz and 0.111 7 Hz, respectively, with an error of 9.0%. However, according to Figure 6(c), with the initial displacement $q_6 = 5°$, the platform yaw of the coupled model is almost consistent with OpenFAST.

The above analysis shows that the natural frequency of yaw affects the roll and the pitch response. This is contrary to the traditional definition of natural frequency, which depends on the inherent characteristics of the system instead of the initial conditions. It can be concluded that the main reason for this phenomenon is attributed to the fact that OpenFAST directly regards the Euler angular velocity vector as the angular velocity, without considering the conversion relationship between them, leading to no decoupling between the rotational DOFs of the platform.

In addition, it can be seen from Figure 5(e) that the tower vibrations of the coupled model are consistent with OpenFAST, except for small differences in amplitude and frequency, mainly because OpenFAST uses the small-angle assumption for the platform transformation matrix partially. As shown in Figure 7, when the platform pitch angle is greater than 10 degrees, the small-angle assumption will cause calculation errors. The extreme values of the platform pitch, tower fore-aft, and blade out-of-plane vibration are all smaller than the calculation results without the small-angle assumption. In addition, the small-angle assumption produces more errors in the estimation of the tower and blade motion responses. For components with high flexibility, the small-angle assumption will produce

Table 1 Comparison of natural frequencies between coupled model and OpenFAST

Degree of freedom	Coupled model (Hz)	OpenFAST (Hz)	Discrepancy (%)
Platform surge	0.008 3	0.008 3	0.00
Platform sway	0.008 3	0.008 3	0.00
Platform heave	0.031 7	0.031 7	0.00
Platform roll	0.033 3	0.033 3	0.00
Platform pitch	0.033 3	0.033 3	0.00
Platform yaw	0.121 7	0.121 7	0.00
Tower fore-aft	0.468 3	0.473 3	1.07
Tower side-side	0.491 7	0.496 7	1.02
Blade flapwise (1st, 2nd, 3rd)	0.700 0, 0.670 0, 0.670 0	0.708 3, 0.678 3, 0.678 3	1.19, 1.24, 1.24
Blade edgewise (1st, 2nd, 3rd)	1.088 3, 1.076 6, 1.076 6	1.101 6, 1.090 0, 1.090 0	1.22, 1.24, 1.24

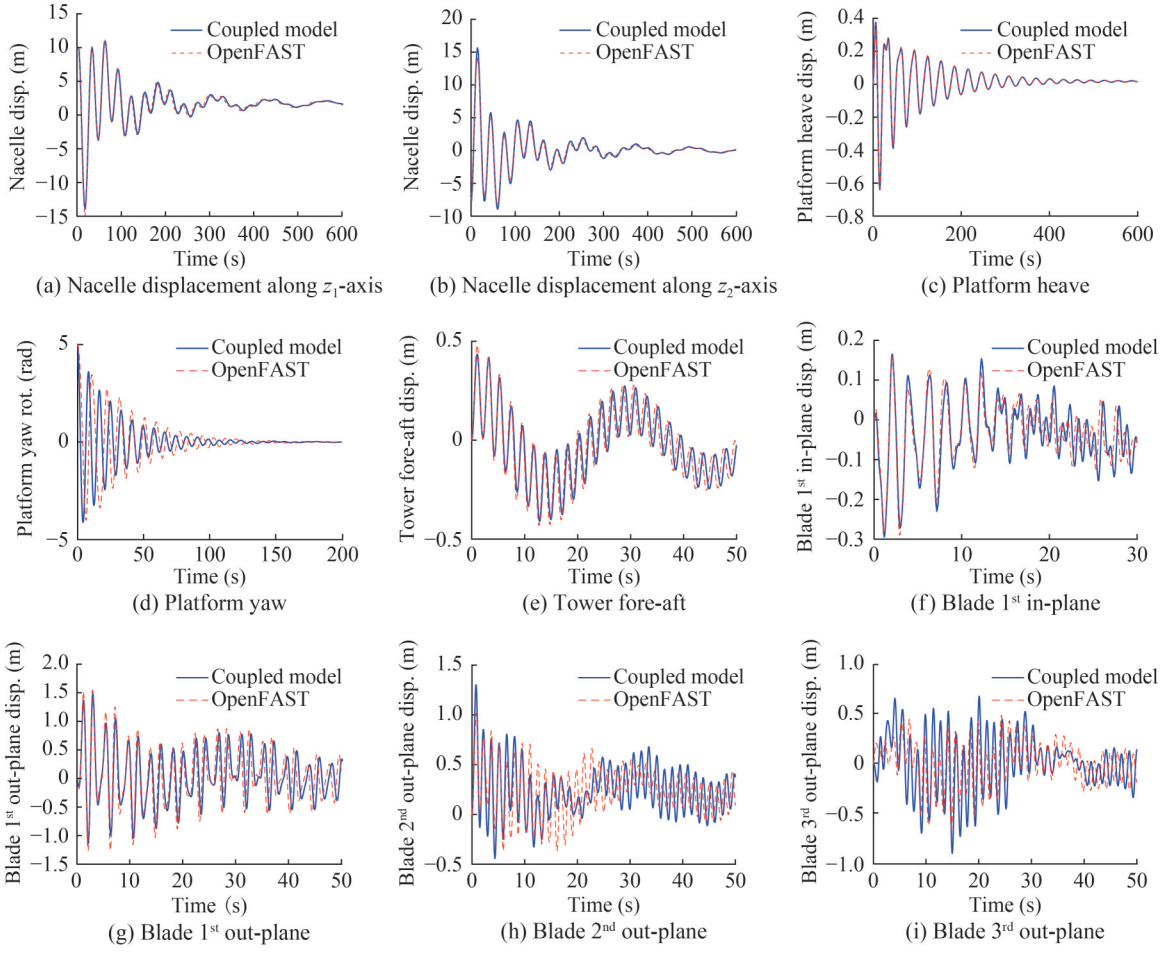


Figure 5 Comparisons of the free vibrations in time-domain

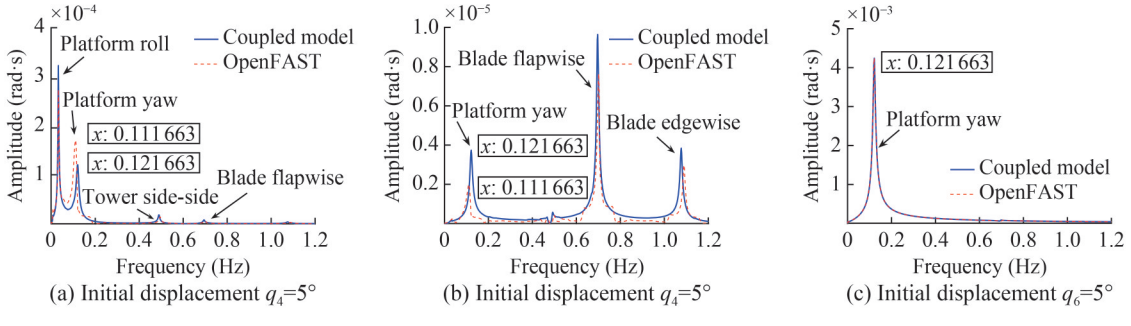


Figure 6 Comparisons of the single-sided amplitude spectrum of the platform yaw

more calculation errors, which will be further analyzed.

In Figure 5, the in-plane vibration of the blade of the model is anastomosed with OpenFAST, while the out-of-plane vibration of the blade is quite different. For comparison, the influence of the platform yaw is removed in Figure 8, when let the model vibrates freely under the initial displacement q_4, q_5 = 5°. Compared with Figure 6, the out-of-plane vibration of blades 2 and 3 are more consistent with the results given by OpenFAST after removing the influence of the platform yaw, which can better indicate that the yaw of platform has a greater impact on the out-plane vibration of the blade. Thus, the model proposed in this paper can be more accurate for the dynamic analysis of the platform under the condition of a large rotation angle.

4.3 Comparison of the FOWT response under wave load

In this part, the system responses under different sea

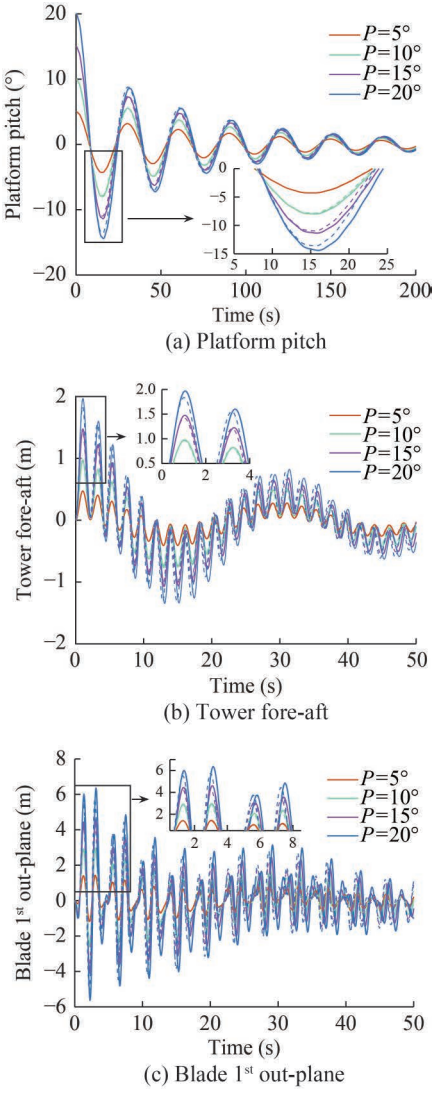


Figure 7 Free vibration responses of the different platform pitch angles (The solid line is the calculation result without the small-angle assumption, and the dotted line is the calculation result with the small-angle assumption)

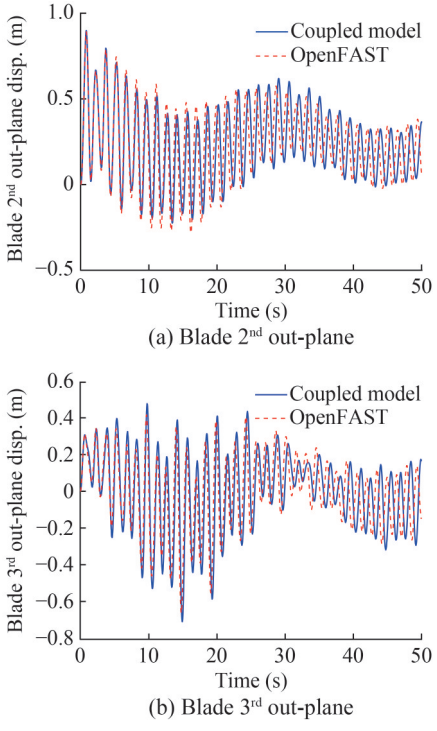


Figure 8 Comparisons of the free vibrations of blade out-plane in time-domain

Table 2 Load cases of wave

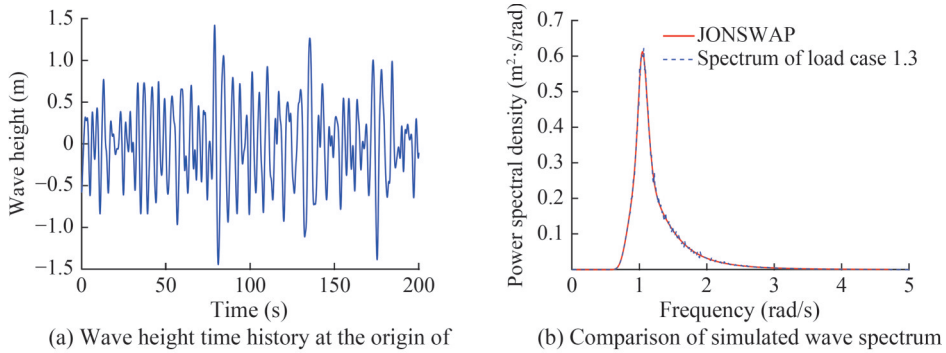
Load case	1.1	1.2	1.3	1.4
Significant wave height (m)	2	0.3	2	5
Spectral period (s)	6	2.5	6	10
Wave spectrum	(-)	(-)	JONSWAP	JONSWAP

conditions along the $\mathbf{z}_1$-axis are compared, as shown in Table 2, to verify the accuracy of the hydrodynamic module and study the effects of the Morison equation and the small-angle assumption. The paper defines four sea conditions, where cases 1.1 and 1.2 represent regular waves, while cases 1.3 and 1.4 represent random waves. The simulated time history of random wave height and the corresponding power spectral density are shown in Figure 9.

Figures 10–12 show the system response of the model under various load cases. It is found that in the three load cases, the system response calculated by the coupling model using the linear potential flow theory is consistent with the results given by OpenFAST, demonstrating the effectiveness and accuracy of the hydrodynamic module.

From Figure 10, it can be seen that the Morison equation can accurately calculate the system response except the platform heave when the ratio of platform diameter to wavelength $D/L \leqslant 0.2$, or the required wave period $T \geqslant 4.56$s. The Morison equation is mainly applicable to the fixed platforms, and the calculation formula of the vertical wave force on the floating platform is not given. Although some researchers modified the Morison equation and gave the calculation method of the vertical wave force (Dinh and Basu, 2015; Al-Solihat et al., 2019), there are still large errors in the platform heave.

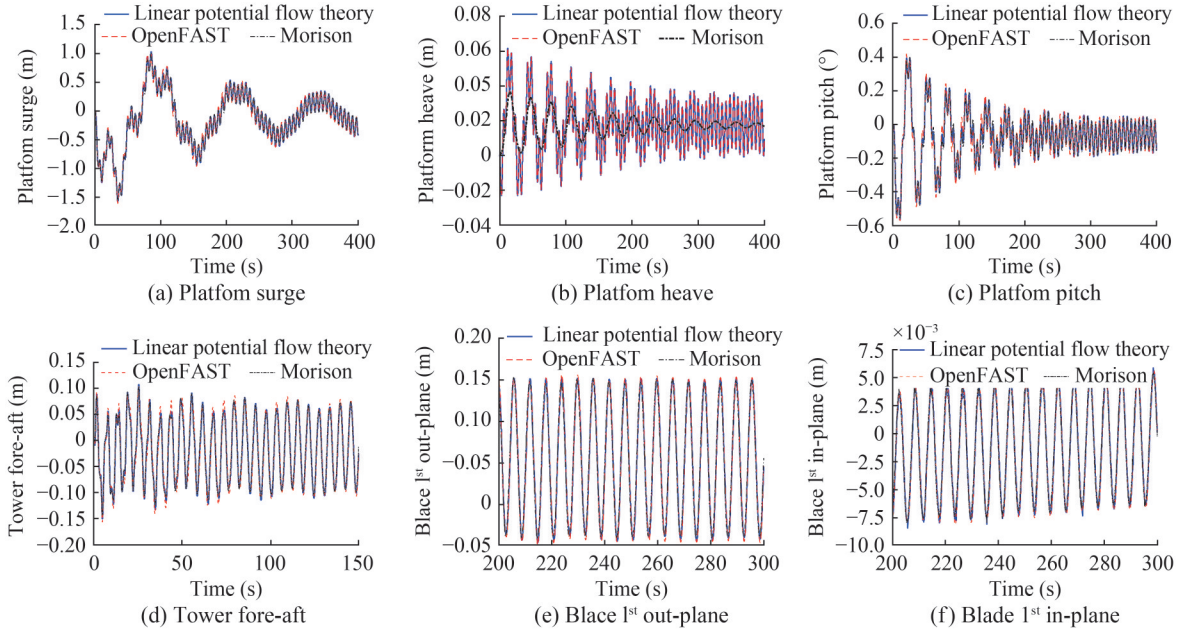
However, it can be noticed from Figure11 that when the wave wavelength exceeds the applicable range of the Morison equation, especially for high-frequency and low-period flexible components such as towers and blades. This is mainly because as the wave period decreases, the wavelength of the wave is no longer significantly greater than the diameter of the platform. When the frequency of the wave is close to the tower frequency, using the Morison equation for calculations may cause resonance of tower, and finally the errors between the blade and the tower will be much larger than that of the platform. As shown in Figure 12, under the action of random waves, the Morison equation similarly overestimates the tower and



(a) Wave height time history at the origin of the global coordinate system

(b) Comparison of simulated wave spectrum and target spectrum

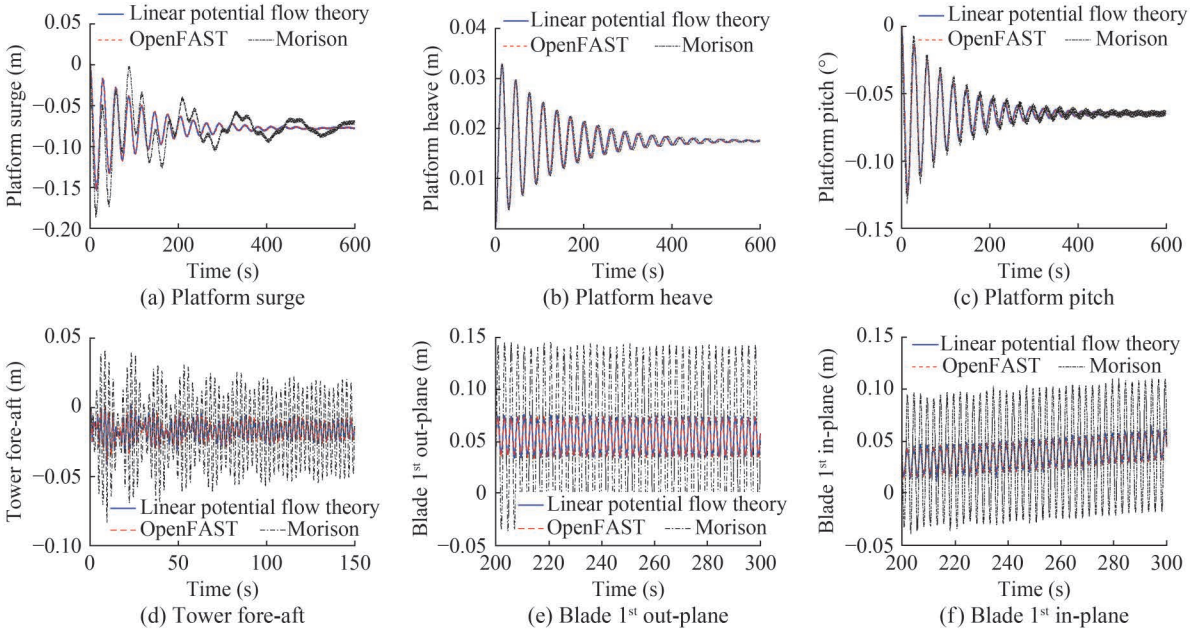
Figure 9 Wave simulation results of load case 1.3



(a) Platfom surge (b) Platfom heave (c) Platfom pitch

(d) Tower fore-aft (e) Blace lst out-plane (f) Blade 1st in-plane

Figure 10 System response of the load case 1.1



(a) Platform surge (b) Platform heave (c) Platform pitch

(d) Tower fore-aft (e) Blade 1st out-plane (f) Blade 1st in-plane

Figure 11 System response of the load case 1.2

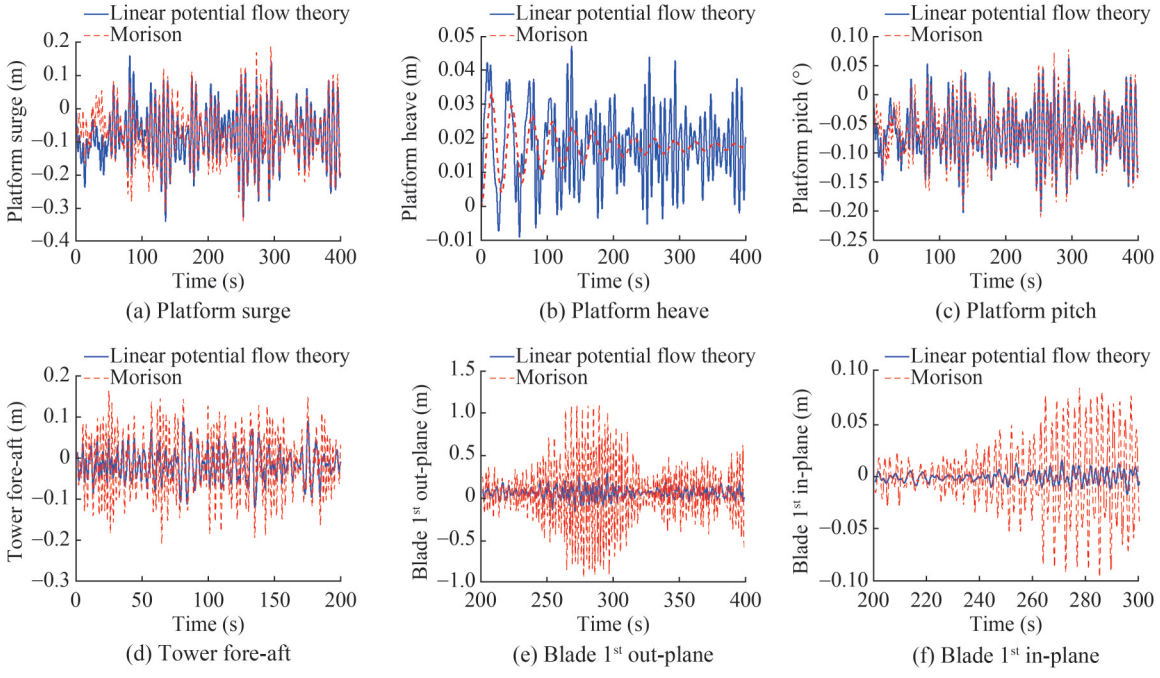


Figure 12 System response of the load case 1.3

blade responses caused by its high-frequency parts. Therefore, compared with the Morison equation, using the linear potential flow theory to calculate the hydrodynamic load of the Spar-type floating platform is more accurate and has a wider range of application.

As shown in Figures 13–14, the system response calculated using the small-angle assumption is smaller than the result without this assumption. In order to study the influence of the small-angle assumption on the calculation results under wave cases, the root mean square (RMS) of the response of each DOF of the system is calculated respectively. When the small-angle assumption is used for calculation, the RMS of the FOWT system's pitch, tower fore-aft, and blade 1st out-plane response are reduced by 4.8%, 24.1%, and 13.5% in load case 1.3, and these values are reduced by 27.7%, 27.9%, and 22.3% in load case 1.4. Therefore, the use of the small-angle assumption will produce larger calculation errors for the flexible components. As the wave load increases, the calculation error will also increase.

4.4 Comparison of the FOWT response under wind load

This part verifies the effectiveness of the aerodynamic force under the turbulent wind, and analyzes the impact of wind turbine control system and the small-angle assumption on the FOWT response. The specific load cases of wind are shown in Table 3. Two different wind spectrum models are employed to simulate the rated wind speed field, and the wind speeds at the hub center of them are shown in Figure 15.

Figures 16 – 17 show the response of the model under load case 2.1 and 2.3. It can be seen from Figure 16(a)–(c) and Figure 17(a) – (c) that the system response calculated by the coupling model using the blade element momentum theory is consistent with the results given by OpenFAST, which verifies that the aerodynamic module of the model

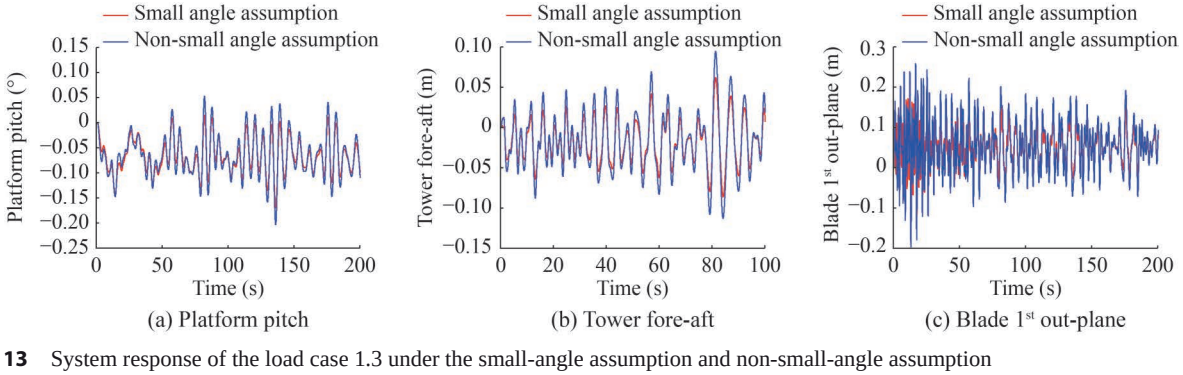
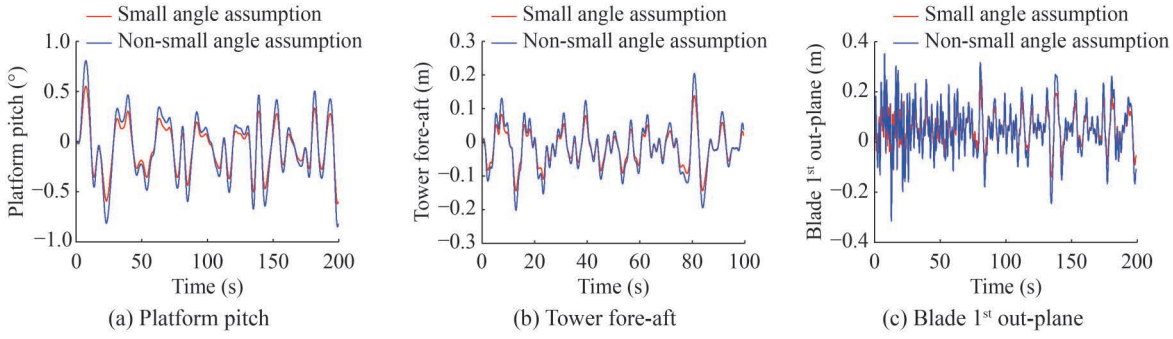


Figure 13 System response of the load case 1.3 under the small-angle assumption and non-small-angle assumption

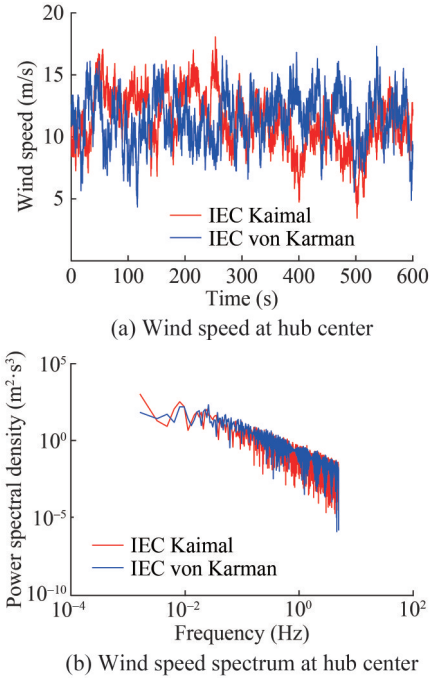


(a) Platform pitch (b) Tower fore-aft (c) Blade 1st out-plane

Figure 14 System response of the load case 1.4 under the small-angle assumption and non-small-angle assumption

Table 3 Load cases of wind

Load case	Mean wind speed (m/s)	Power law exponent	Turbulence model	Turbulence characteristic
2.1	11.4	0.14	IEC Kaimal	0.16
2.2	30			0.20
2.3	11.4		IEC von Karman	0.16



(a) Wind speed at hub center

(b) Wind speed spectrum at hub center

Figure 15 Comparison of wind speeds of load cases 2.1 and 2.3

is effective and can accurately calculate the aerodynamic load of the blade. Because the FOWT is subjected to variable wind thrust, its response along the $\boldsymbol{z}_1$-axis also exhibits significant fluctuations. In addition, it can be seen from Figure 16(d)−(f) and Figure 17(d)−(f) that the results of variable speed control (VS) and pitch control (PC) of the coupled model are consistent with those of OpenFAST. Meanwhile, after considering the VS and PC, the coupled model can accurately simulate the rotor speed and power output of the FOWT during operation with different wind fields, which is more suitable for the actual situation.

As shown in Figure 16(d)–(e), the rotor speed and the generating power are both larger than the set rated values, because the control strategy in region 3, as shown in Figure 3, has been changed from constant power generation to constant torque. The rotor speed and generating power of the system under the two different variable speed control strategies are shown in Figure 18. It can be seen that the rotor speed under constant power is significantly greater than the rotor speed at constant torque, and the stability of constant power is also poor. However, this improvement can overload the generator and generate power beyond the rated value for a short time.

It can be seen from Figure 18 that the rotor speed and power of the FOWT are not maintained at the set rated value, but change with the change of the wind speed. Therefore, if the change of the rotor speed is ignored, the DOF of the generator q_{10} will be cancelled, which may have a certain impact on the system response. As shown in Figure 19, the influence of the generator's DOF on system response under load case 2.1 is studied. It can be found that when the system ignores the DOF of the generator, and the random wind is higher than the rated wind speed, the error of the system response cannot be ignored. In addition, the system with PC can maintain the rotor speed at the rated speed and effectively reduce the system response. Therefore, considering the DOF of generator is necessary for accurate calculation of the system response and deeper research on mechanical control, such as PC and VS.

In addition, to study the effect of the small-angle assumption on the simulated FOWT motion under wind load, the calculation results of the small-angle assumption and non-small-angle assumption under load cases 2.1 and 2.2 are compared, which represent the normal operating condition and the extreme condition, respectively. The cut-out wind speed of the 5 MW reference wind turbine of NREL is 25 m/s. In order to avoid excessive damage to the FOWTs caused by ambient wind, the rotor is forced to stop running. The shutdown load case can be simulated by disabling the generator's DOF, assuming that the rotor speed is always 0, and turning off the control system. In addition, the influence of the wake should be ignored in aerodynamic calculation. That is, both the axial induction fac-

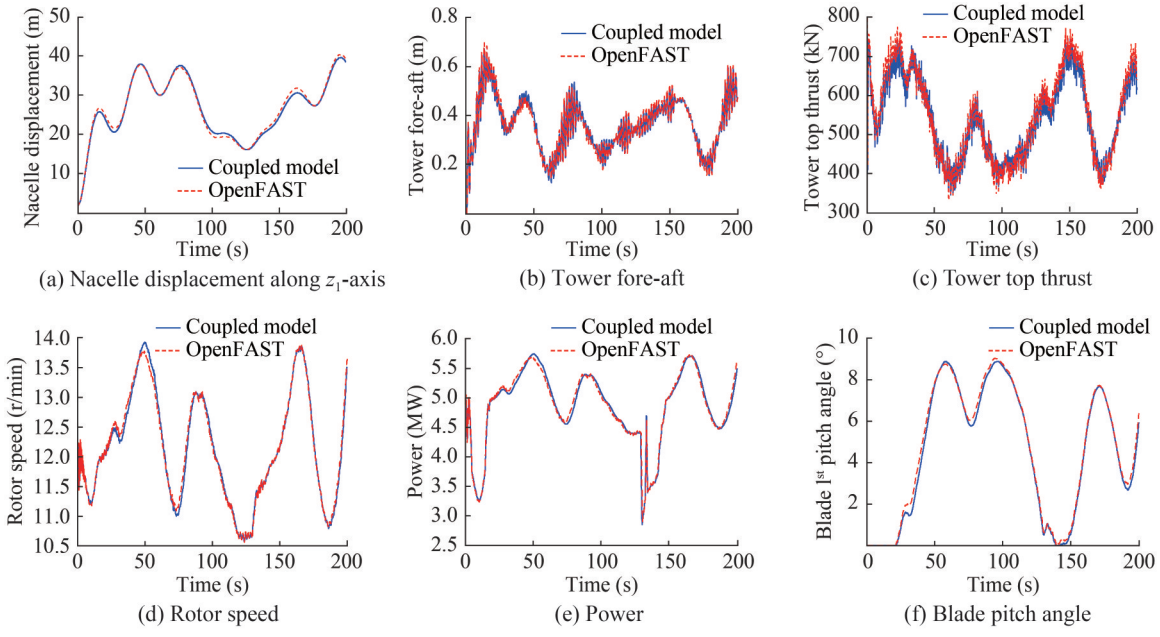


Figure 16 System response of the load case 2.1

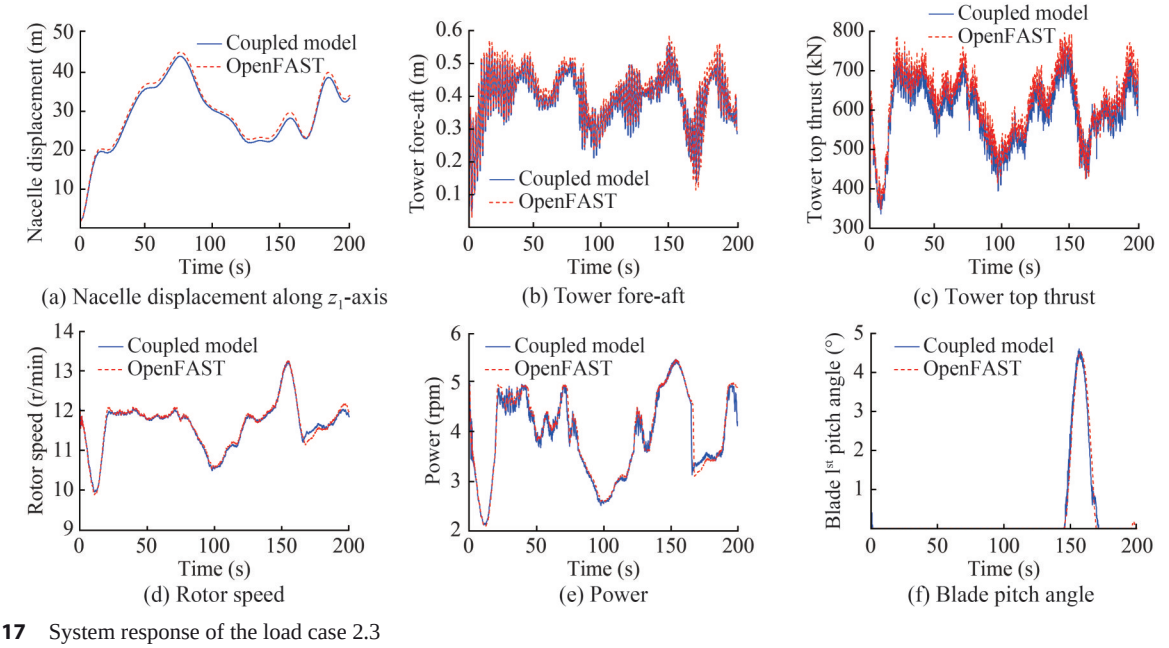


Figure 17 System response of the load case 2.3

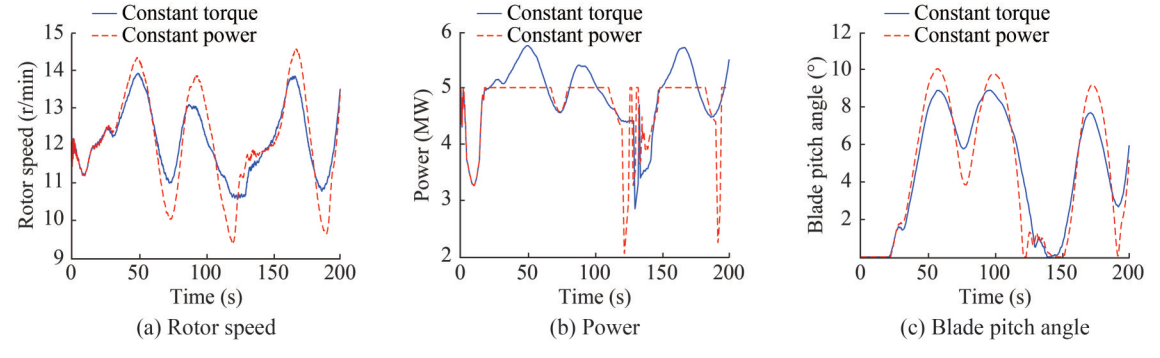


Figure 18 Comparison of system response under two different variable speed control strategies

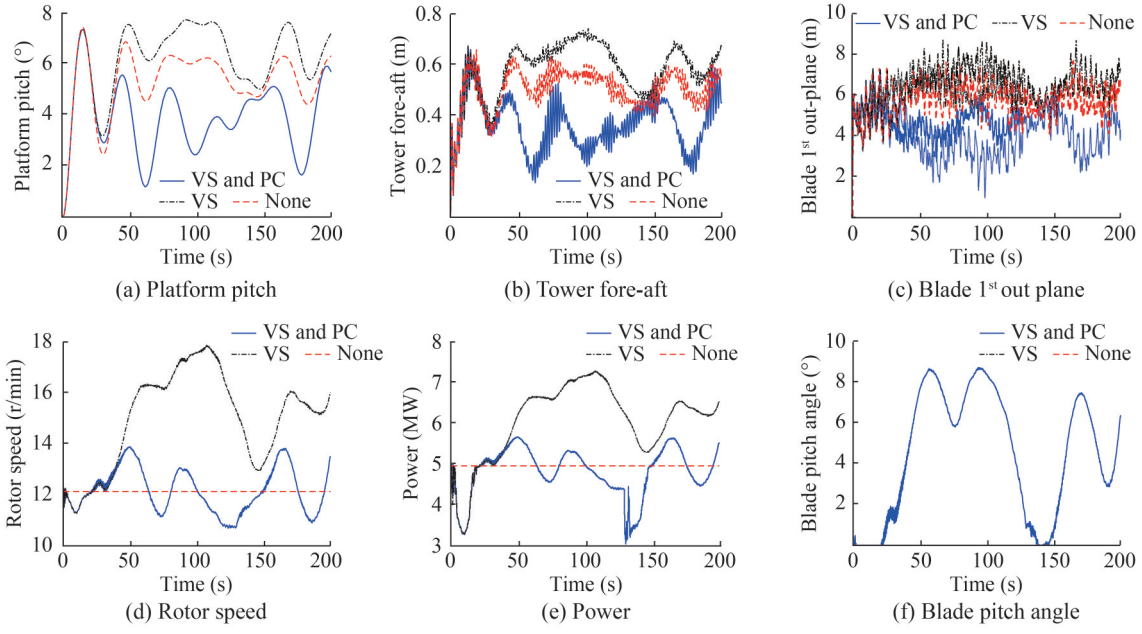


Figure 19 Influence of the generator's DOF on system response under load case 2.1

tor a and the tangential induction factor a' are assumed as zero.

Figures 20–21 show that using the small-angle assumption when calculating the response of a FOWT under wind loads will result in a larger estimate. Under load case 2.1, the pitch and tower fore-aft responses of the system calculated using the small-angle assumption are more severe in the initial stage, and they are consistent with the results using the non-small-angle assumption after 150 s. In terms of the blade 1st out-plane response, the small-angle assumption has a greater impact on the simulation of high-frequency vibration, and the results are quite different from those with the non-small-angle assumption. Under load case 2.2, the calculation using the small-angle assumption will generally increase the system pitch, tower fore-aft, and blade 1st out-plane responses.

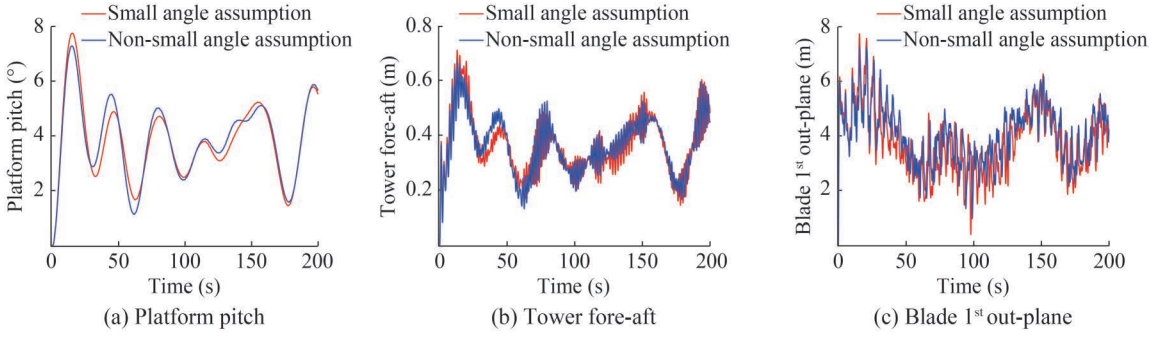


Figure 20 System response of the load case 2.1 under the small-angle assumption and non-small-angle assumption

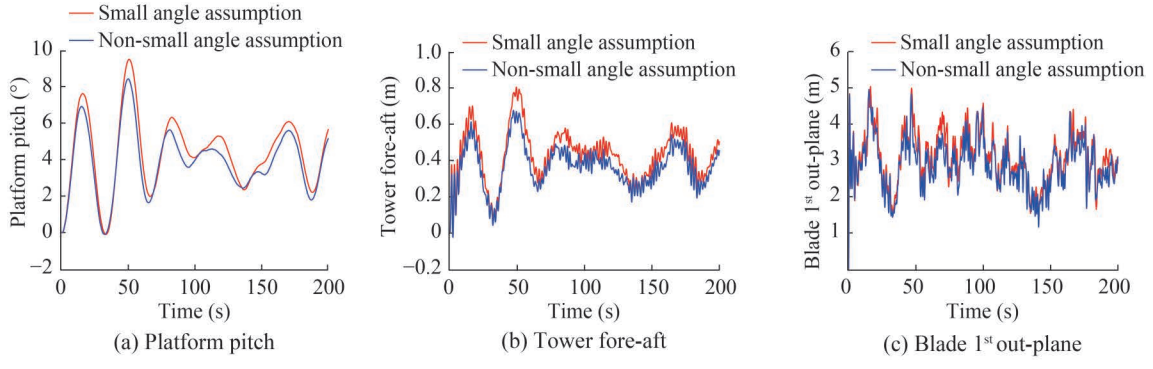


Figure 21 System response of the load case 2.2 under the small-angle assumption and non-small-angle assumption

5 Effect of the small-angle assumption on the application of the TSMD in the FOWT

According to the previous analysis, when the pitch angle of the FOWT is large, using the small-angle assumption will cause errors. Similarly, for some applications of the FOWT, the error caused by the small-angle assumption should also be considered. This section takes the TSMD proposed by Jahangiri and Sun (2020) as an example, as shown in Figure 22, and uses the strict coordinate rotation matrix to establish the motion equation of the TSMD to analyze the error caused by the small-angle assumption. When the FOWT is loaded in the *X*-axis direction, the TSMD also swings in the same direction. To simplify the calculation, it is assumed that the TSMD can only swing around the *Y*-axis, so the position vector and angular velocity vector of the TSMD in the inertial coordinate system are represented in Eqs. (65) and (66).

$$\boldsymbol{r}_{\mathrm{ts}}(t)=\begin{Bmatrix}q_1\\q_2\\q_3\end{Bmatrix}+\boldsymbol{R}_{\mathrm{p}}^{\mathrm{T}}\begin{Bmatrix}q_7\\q_8\\h_{\mathrm{t}}+h_{\mathrm{b}}-v_{\mathrm{t}}(h_t,t)\end{Bmatrix}+\boldsymbol{R}_{\mathrm{p}}^{\mathrm{T}}\boldsymbol{R}_{\mathrm{t}}^{\mathrm{T}}\boldsymbol{R}_{\mathrm{ts}}^{\mathrm{T}}\begin{Bmatrix}0\\0\\-\rho\end{Bmatrix} \tag{65}$$

$$\boldsymbol{\omega}_{\mathrm{ts}}(t)=\boldsymbol{T}_{\mathrm{p}}^{-1}\begin{Bmatrix}q_4'\\q_5'\\q_6'\end{Bmatrix}+\boldsymbol{R}_{\mathrm{p}}^{\mathrm{T}}\boldsymbol{T}_{\mathrm{t}}^{-1}\begin{Bmatrix}\theta_{\mathrm{SS}}'\\\theta_{\mathrm{FA}}'\\0\end{Bmatrix}+\boldsymbol{R}_{\mathrm{p}}^{\mathrm{T}}\boldsymbol{R}_{\mathrm{t}}^{\mathrm{T}}\begin{Bmatrix}0\\q_{17}'\\0\end{Bmatrix} \tag{66}$$

where R_{ts} is the coordinate rotation matrix corresponding to the swing angle $\{0, q_{17}, 0\}$ of the mass ball. ρ is the swing radius of the mass ball.

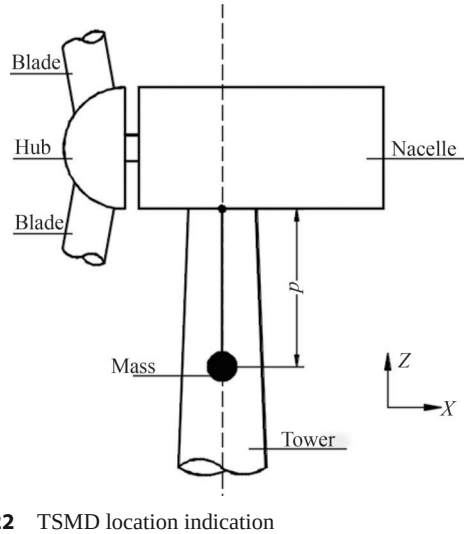


Figure 22 TSMD location indication

The kinetic energy, potential energy, and damping coefficient of the FOWT with the TSMD are:

$$T_{\mathrm{con}}=T+\frac{1}{2}m_{\mathrm{ts}}\boldsymbol{v}_{\mathrm{ts}}^{\mathrm{T}}\boldsymbol{v}_{\mathrm{ts}}+\frac{1}{2}\boldsymbol{\omega}_{\mathrm{ts}}^{\mathrm{T}}\boldsymbol{J}_{\mathrm{ts}}\boldsymbol{\omega}_{\mathrm{ts}} \tag{67}$$

$$V_{\mathrm{con}}=V+m_{\mathrm{ts}}g\boldsymbol{r}_{\mathrm{ts}}\cdot\begin{pmatrix}0&0&1\end{pmatrix}^{\mathrm{T}} \tag{68}$$

$$c_{\mathrm{ts}}=2\zeta_{\mathrm{ts}}m_{\mathrm{ts}}\omega_7 \tag{69}$$

where m_{ts} is the mass of the ball ($m_{\mathrm{ts}}=\lambda_{\mathrm{ts}}(m_{\mathrm{n}}+m_{\mathrm{h}})$, λ_{ts} is the mass ratio). $\boldsymbol{J}_{\mathrm{ts}}$ is the moment of inertia of the mass ball. ξ_{ts} is the damping ratio of the TSMD, which is taken as 1% in this section. ω_7 is the natural circle frequency of the tower fore-aft vibration under uncontrolled conditions.

5.1 Analysis of the TSMD vibration reduction effect

Since the Spar FOWT relies on the ballast in the platform for stability, a TSMD with excessively large mass will bring FOWT's center of gravity closer to the surface of water and have a bad effect. Therefore, in this section, the FOWT's displacement response of the tower fore-aft is calculated by considering three TSMD's mass ratios such as 1%, 2%, and 3% under the following conditions: case 5.1 is the free vibration with initial displacement q_7 = 0.5 m; case 5.2 is random wave load along $\boldsymbol{z}_1$-axis with significant wave height of 0.3 m and spectral period of 2.5 s; case 5.3, which is same as case 1.3, and case 5.4, which is same as case 2.1.

The exhaustive method is used to determine the optimal swing radius for the vibration reduction effect of the tower fore-aft under different load cases, including 1.2 m for working case 5.1, 1.1 m for working cases 5.2 and 5.3, and 0.85 m for working case 5.4. Figure 23(a)−(d) show that when the FOWT's tower is in the state of free vibration or the frequency of the dynamic load is close to the natural frequency of the tower fore-aft DOF, the vibration response of the tower fore-aft DOF can be effectively reduced by adjusting the TSMD swing radius. In Figure 23(e)−(f), when the frequency of wave is different from that of the tower fore-aft vibration, TSMD can significantly reduce the spectrum amplitude of the tower fore-aft vibration displacement at the frequency of the tower fore-aft vibration, but this part is not the main component in the displacement spectrum. In the displacement time history, TSMD has a certain damping effect only in the early stage of the movement, but the control effect is not obvious in the subsequent motion. It can be seen from Figure 23(g)−(h) that the displacement of the tower fore-aft vibration under the wind load is composed of low-frequency vibration and high-frequency vibration, and the TSMD placed on the top of the tower only has a certain control effect on the high-frequency vibration part, and the control effect on the low-frequency vibration is not ideal.

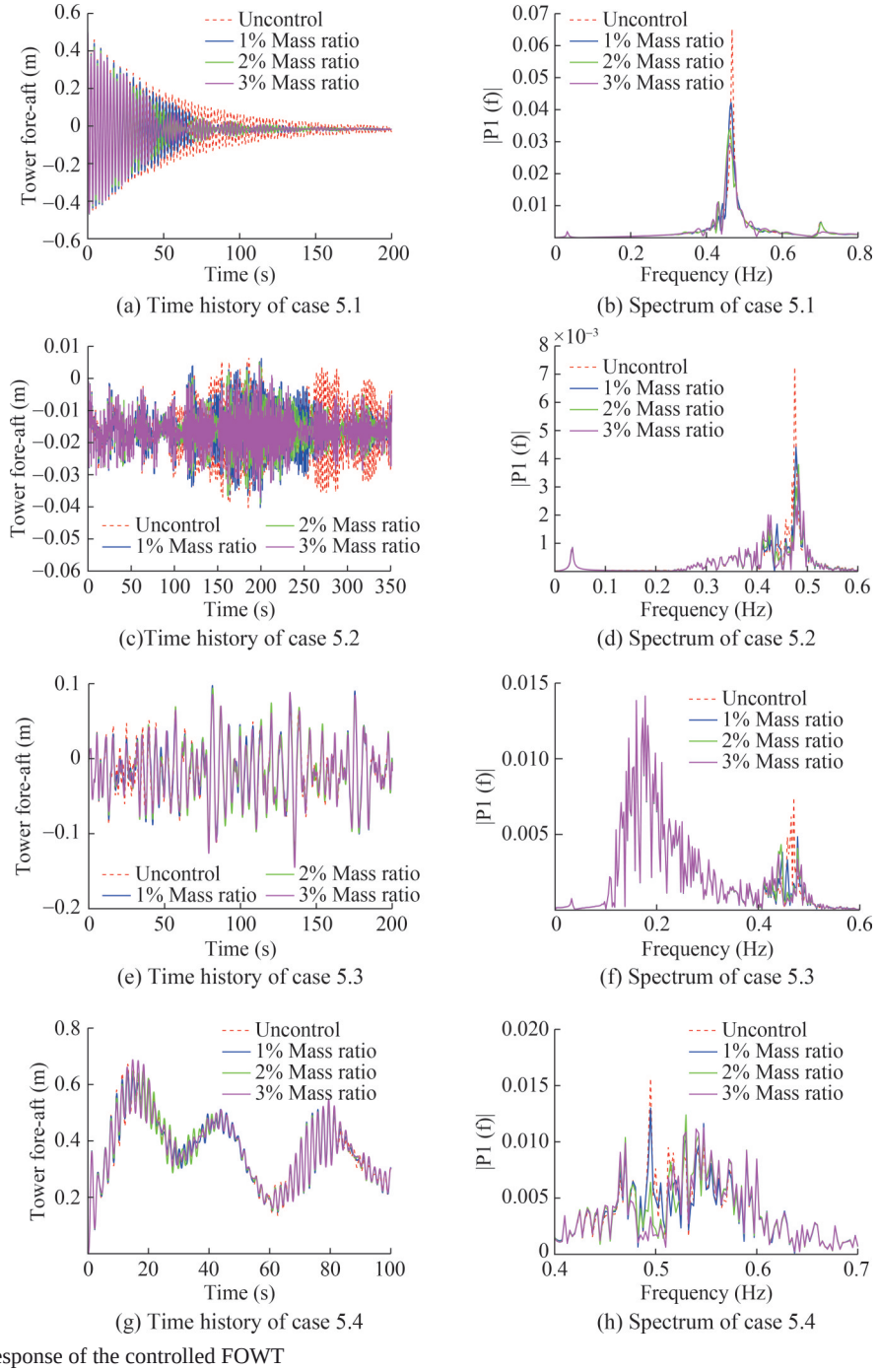


Figure 23 7th DOF response of the controlled FOWT

5.2 Comparison of TSMD vibration damping performance under the small-angle assumption and non-small-angle assumption

When the strict coordinate rotation matrix mentioned above is used to establish the motion equation of the FOWT including TSMD, complex non-quadratic terms will be generated, which increase the difficulty of solution and the computational cost. Therefore, the equation of motion can be simplified by making the small-angle assumption ($\sin(q_{17}) \approx q_{17}$, $\cos(q_{17}) \approx 1$, $q'^2_{17} \approx 0$). Based on the FOWT's equation of motion with simplified TSMD by the small-angle assumption, in this section, the dynamic response of the controlled structure under the four load cases in Section 5.1 is calculated, and a comparison with the calculation results under the non-small-angle assumption is conducted to determine the influence of the small-angle assumption on TSMD's vibration reduction performance. In order to understand the impact of the small-angle assumption on the vibration reduction performance

of the TSMD, the displacement two-norm coefficient is introduced as the evaluation criterion, which can be defined as follows:

$$\delta = \left| \frac{N - N'}{N} \right| \times 100\% \tag{70}$$

$$N = \left(|x_1|^2 + |x_2|^2 + \cdots + |x_n|^2 \right)^{1/2} \tag{71}$$

$$N' = \left(|x_1'|^2 + |x_2'|^2 + \cdots + |x_n'|^2 \right)^{1/2} \tag{72}$$

where N, N' are the two-norm coefficients of the displacement responses of controlled structures under external excitation with the non-small-angle assumption and the small-angle assumption, respectively; x_i, x_i' are the displacement responses of controlled structures under external excitation with the non-small-angle assumption and the small-angle assumption, respectively.

It can be seen from Figure 24, when using the small-angle assumption, the tower fore-aft displacement of the controlled FOWT with 3% mass ratio is smaller than that of the non-small-angle assumption. So, using the small-angle assumption to calculate the TSMD model will get a better control effect. Then, the swing angle of the TSMD with the small-angle assumption is larger than that of the non-small-angle assumption at the initial stage of motion, indicating that the response of the TSMD is more intense and corresponds to the smaller vibration of the tower fore-aft. Therefore, the small-angle assumption can be used to describe the motion of the TSMD relatively accurate, but it will increase the vibration reduction effect of the TSMD. In order to study the influence of the small-angle assumption on the vibration reduction effect of the TSMD, the displacement responses of controlled FOWTs with different mass ratio TSMDs under four load cases are compared, as shown in Table 4.

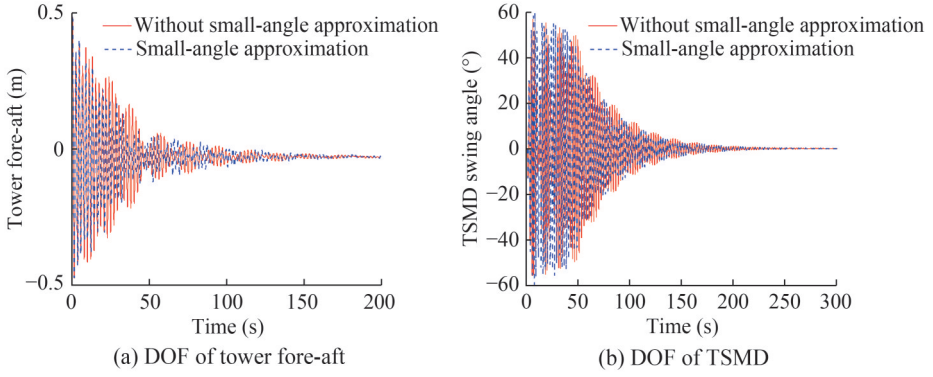


Figure 24 Displacement response of controlled FOWT with 3% mass ratio

Table 4 FOWT displacement response

Load case (mass ratio)	Maximum displacement of tower fore-aft		δ_7 (%)	Maximum swing angle of TSMD		δ_{17} (%)
	Small-angle assumption (m)	Non-small- angle assumption (m)		Small-angle assumption (°)	Non-small-angle assumption (°)	
5.1 (1%)	–	–	2.610	55.93	52.23	4.35
5.1 (2%)	–	–	3.670	59.80	54.59	6.82
5.1 (3%)	–	–	14.690	60.06	57.42	8.85
5.2 (1%)	0.0059	0.0059	0.091	6.51	6.47	0.55
5.2 (2%)	0.0034	0.0048	1.230	4.95	4.66	7.67
5.2 (3%)	0.0025	0.0038	0.430	5.99	4.52	13.98
5.3 (1%)	0.1048	0.1054	0.049	10.84	10.95	0.87
5.3 (2%)	0.1066	0.1064	0.071	10.75	10.63	2.42
5.3 (3%)	0.1062	0.1058	0.013	8.87	8.95	0.89
5.4 (1%)	0.6600	0.6900	0.037	52.47	18.17	113
5.4 (2%)	0.6900	0.6900	0.018	28.39	15.78	70.07
5.4 (3%)	0.7000	0.7000	0.030	24.32	15.16	55.37

It can be seen from Table 4 that when the vibration displacement of the tower is small, the calculation error of the small-angle assumption on the DOF of the TSMD swing angle can be ignored, but when the tower fore-aft displacement exceeds a certain limit, the error can't be ignored. If the main frequency of the tower fore-aft vibration displacement is close to the TSMD swing frequency, the calculation error of the small-angle assumption on the TSMD swing displacement is greater with the increase of the mass ratio, so the error caused by the small-angle assumption can't be ignored when calculating results of the TSMD with large mass ratio. On the other hand, when the FOWT is subjected to wind load, the calculation results of the TSMD swing displacement are very different between the small-angle and non-small-angle assumptions. Thus, it is not recommended to use the small-angle assumption to simplify the calculation when considering to reduce wind-induced vibration of FOWT.

6 Conclusion

In this paper, an improved 16-DOF coupled dynamic model of the Spar-type FOWT under complex working conditions was established to accurately calculate its dynamic response, including aerodynamic, hydrodynamic structural analysis and control modules, etc. The influence of small-angle assumptions on the calculation accuracy for the coupling model and the mass damper in the FOWT was evaluated. The main conclusions obtained are summarized as follows:

(1) Instead of the small-angle assumption, introducing the strict rotation matrix and the transformation relationship between the angular velocity and Euler-angular velocity, the model is more suitable for the dynamic analysis of the platform under the condition of large rotations, and can more accurately simulate the system response, with a wider applicability. At the same time, considering the control of the power generation system and the PC control is more suitable for the actual situation of the FOWT operation.

(2) Compared with the linear potential flow theory, the Morison equation is applicable within a limited range, and when the period of the wave load is small, the Morison equation will overestimate the response of the FOWT tower and blades caused by the high-frequency components of the wave. Therefore, for random wave containing multiple frequency components, the wave loads generated by it are more accurately calculated using the linear potential flow theory.

(3) Using the small-angle assumption in the calculation of the FOWT will produce certain errors. When the swing angle of the FOWT platform exceeds 10 degrees, the small-angle assumption will cause calculation errors and affect the calculation of the upper flexible structure response. For wave action, the use of the small-angle assumption will underestimate the load, making the response of the FOWT smaller than that using the non-small-angle assumption, and this error increases with the increase of significant wave height. Under wind load, the small-angle assumption will lead to large errors in estimating the high-frequency vibration of the flexible structures such as towers and blades. At the same time, when the FOWT is shut down in extreme case, the small-angle assumption will overestimate the peak value of its response.

(4) The TSMD located at the top of tower has good control effect on the frequency components close to the natural frequency of the FOWT's tower fore-aft DOF. However, if the calculation uses the small-angle assumption, the calculated oscillator displacement will be greater than the calculated value without the small-angle assumption, as the TSMD swing angle increases, which will lead to an erroneous estimation of the control effect. When the FOWT is subjected to the wind load, the tower vibration response is violent, and the TSMD swing angle calculated using the small-angle assumption is significantly different from that calculated without this assumption. Therefore, it is not recommended to use the small-angle assumption when evaluating the mass damper control effect for the FOWT.

Funding The National Natural Science Foundation of China (Grant No. 52378313).

Competing interests The authors have no competing interests to declare that are relevant to the content of this article.

References

Al-Solihat MK, Nahon M, Behdinan K (2019) Dynamic modeling and simulation of a spar floating offshore wind turbine with consideration of the rotor speed variations. Journal of Dynamic Systems, Measurement, and Control 141(8): 081014. https://doi.org/10.1115/1.4043104

Cacciuttolo C, Navarrete M, Atencio E (2024) Renewable wind energy implementation in South America: A comprehensive review and sustainable prospects. Sustainability 16(14): 6082. https://doi.org/10.3390/su16146082

Chang T, Peng YB (2025) Hybrid vibration control of floating offshore wind turbine structure considering multi-directional waves. Ocean Engineering 335: 121533. https://doi.org/10.1016/j.oceaneng.2025.121533

Chen JH, Hu ZQ, Liu GL, Wan DC (2019) Coupled aero-hydro-servo-elastic methods for floating wind turbines. Renewable energy 130: 139-153. https://doi.org/10.1016/j.renene.2018.06.060

Chopra AK (2007) Dynamics of structures. USA: Pearson Education India, New Jersey

Dinh VN, Basu B (2015) Passive control of floating offshore wind turbine nacelle and spar vibrations by multiple tuned mass dampers. Structural Control and Health Monitoring 22(1): 152-176. https://doi.org/10.1002/stc.1666

DNV GL (2016) Bladed theory mnual (Version 4.8). Garrad Hassan &

Partners, Bristol, UK
Edwards EC, Holcombe A, Brown S, Ransley E, Hann M, Greaves D (2023) Evolution of floating offshore wind platforms: A review of at-sea devices. Renewable and Sustainable Energy Reviews 183: 113416. https://doi.org/10.1016/j.rser.2023.113416
Edwards EC, Holcombe A, Brown S, Ransley E, Hann M, Greaves D (2024) Trends in floating offshore wind platforms: A review of early-stage devices. Renewable and Sustainable Energy Reviews 193: 114271. https://doi.org/10.1016/j.rser.2023.114271
Evro S, Veith J, Akinwale A, Tomomewo OS (2025) Enhancing floating offshore wind turbine systems through multi-scale coupled modeling. Sustainable Energy Technologies and Assessments 77: 104299. https://doi.org/10.1016/j.seta.2025.104299
Falcão JP, Brito JLVD, Avila SM, Morais MVGD (2023) Passive control by inverted pendulum of a floating offshore wind turbine. International Journal of Structural Stability Dynamics 23(9): 2350101. https://doi.org/10.1142/S0219455423501018
Fossen TI (2011) Handbook of marine craft hydrodynamics and motion control. UK: John Wiley & Sons, West Sussex
Hannan MA, Al-Shetwi AQ, Mollik MS, Ker PJ, Mannan M, Mansor M, Al-Masri HMK, Mahlia TMI (2023) Wind energy conversions, controls, and applications: A review for sustainable technologies and directions. Sustainability 15(5): 3986. https://doi.org/10.3390/su15053986
He J, Jin X, Xie SY, Cao L, Lin YF, Wang N (2019) Multi-body dynamics modeling and TMD optimization based on the improved AFSA for floating wind turbines. Renewable Energy 141: 305-321. https://doi.org/10.1016/j.renene.2019.04.005
Higgins CW, Froidevaux M, Simeonov V, Vercauteren N, Barry C, Parlange MB (2012) The effect of scale on the applicability of Taylor's frozen turbulence hypothesis in the atmospheric boundary layer. Boundary-layer Meteorology 143: 379-391. https://doi.org/10.1007/s10546-012-9701-1
Høeg CE, Zhang ZL (2021) The influence of gyroscopic effects on dynamic responses of floating offshore wind turbines in idling and operational conditions. Ocean Engineering 227: 108712. https://doi.org/10.1016/j.oceaneng.2021.108712
Hu YQ, He EM (2017) Active structural control of a floating wind turbine with a stroke-limited hybrid mass damper. Journal of Sound and Vibration 410: 447-472. https://doi.org/10.1016/j.jsv.2017.08.050
Jahangiri V, Sun C (2020) Three-dimensional vibration control of offshore floating wind turbines using multiple tuned mass dampers. Ocean Engineering 206: 107196. https://doi.org/10.1016/j.oceaneng.2020.107196
Jonkman B, Kilcher L (2012) TurbSim user's guide: version 1.06.00. National Renewable Energy Laboratory (NREL), Golden, United States
Jonkman J (2003) Modeling of the UAE wind turbine for refinement of FAST_AD. National Renewable Energy Laboratory (NREL), Golden, United States, Technical Report No. NREL/TP-500-34755
Jonkman J, Buhl ML (2005) FAST user's guide. National Renewable Energy Laboratory (NREL), Golden, United States, Technical Report No. NREL/EL-500-38230
Jonkman J (2009) Dynamics of offshore floating wind turbines-model development and verification. Wind Energy: An International Journal for Progress and Applications in Wind Power Conversion Technology 12(5): 459-492. https://doi.org/10.1002/we.347
Jonkman J, Butterfield S, Musial W, Scott G (2009) Definition of a 5 MW reference wind turbine for offshore system development. National Renewable Energy Laboratory (NREL), Golden, United States, Technical Report No. NREL/TP-500-38060
Jonkman J, Matha D (2010) Quantitative comparison of the responses of three floating platforms. National Renewable Energy Laboratory (NREL), Golden, United States, Technical Report No. NREL/CP-500-46726
Jonkman J (2010) Definition of the floating system for Phase IV of OC3. National Renewable Energy Laboratory (NREL), Golden, United States, Technical Report No. NREL/TP-500-47535
Larsen TJ, Hansen AM (2014) How 2 HAWC2, the user's manual. Risø National Laboratory, Technical University of Denmark, Roskilde, Denmark, Technical Report Risø-R-1597(ver. 4-7) (EN)
Larsen TJ, Hanson TD (2007) A method to avoid negative damped low frequent tower vibrations for a floating, pitch controlled wind turbine. Journal of Physics: Conference Series 75(1): 012073. https://doi.org/10.1088/1742-6596/75/1/012073
López-Queija J, Robles E, Jugo J, Alonso-Quesada S (2022) Review of control technologies for floating offshore wind turbines. Renewable and Sustainable Energy Reviews 167: 112787. https://doi.org/10.1016/j.rser.2022.112787
Luo YF, Sun HX, Hall L, Lambert D, Okuda R, Wang WX, Fang B, Zuo L (2024) Vibration control for a semi-submersible floating offshore wind turbine with optimal ultra-low frequency electromagnetic tuned inerter-mass dampers. Structures 63: 106296. https://doi.org/10.1016/j.istruc.2024.106296
Mirtich BV (1996) Impulse-based dynamic simulation of rigid body systems. University of California, Berkeley
Mu AL, Huang ZB, Liu AB, Yang B, Wang JH, Qian Ye, Wang H (2022) Bluff body vortex-induced vibration control of floating wind turbines based on a novel intelligent robust control algorithm. Physics of Fluids 34(11): 114103. https://doi.org/10.1063/5.0121829
Ning SA, Hayman G, Damiani R, Jonkman J (2015) Development and validation of a new blade element momentum skewed-wake model within AeroDyn. AIAA Science and Technology Forum and Exposition, Florida, United States
Ojo A, Collu M, Coraddu A (2022) Multidisciplinary design analysis and optimization of floating offshore wind turbine substructures: A review. Ocean Engineering 266: 112727. https://doi.org/10.1016/j.oceaneng.2022.112727
Olabi AG, Obaideen K, Abdelkareem MA, AlMallahi MN, Shehata N, Alami AH, Mdallal A, Hassan AAM, Sayed ET (2023) Wind energy contribution to the sustainable development goals: Case study on London array. Sustainability 15(5): 4641. https://doi.org/10.3390/su15054641
Ormberg H, Passano E, Luxcey N (2011) Global analysis of a floating wind turbine using an aero-hydro-elastic model: Part 1-code development and case study. ASME 2011 30th International Conference on Ocean, Offshore and Arctic Engineering, Rotterdam, Netherlands, 5: 837-847
Pérez-Collazo C, Greaves D, Iglesias G (2015) A review of combined wave and offshore wind energy. Renewable and Sustainable Energy Reviews 42: 141-153. https://doi.org/10.1016/j.rser.2014.09.032
Ramakrishnan S, Delpisheh M, Convery C, Niblett D, Vinothkannan M, Mamlouk M (2024) Offshore green hydrogen production from wind energy: Critical review and perspective. Renewable and Sustainable Energy Reviews 195: 114320. https://doi.org/10.1016/j.rser.2024.114320
Shinozuka M, Deodatis G (1991) Simulation of stochastic processes by spectral representation. Applied Mechanics Reviews 44(4): 191-204. https://doi.org/10.1115/1.3119501

Si YL, Karimi HR, Gao HJ (2014) Modelling and optimization of a passive structural control design for a spar-type floating wind turbine. Engineering Structures 69: 168-182. https://doi.org/10.1016/j.engstruct.2014.03.011

Stewart G, Lackner M (2013) Offshore wind turbine load reduction employing optimal passive tuned mass damping systems. IEEE Transactions on Control Systems Technology 21(4): 1090-1104. https://doi.org/10.1109/TCST.2013.2260825

Su X, Wang XD, Xu WL, Yuan LQ, Xiong CH, Chen JM (2024) Offshore wind power: Progress of the edge tool, which can promote sustainable energy development. Sustainability 16(17): 7810. https://doi.org/10.3390/su16177810

Sun YT, Li SJ, Chen MM, Wang RB, Zhao Y (2025) Statistical linearization of nonlinear coupled system of floating offshore wind turbine under wind and wave excitation and application. Ocean Engineering 341: 122604. https://doi.org/10.1016/j.oceaneng.2025.122604

Tian HN, Soltani MN, Nielsen ME. (2023) Review of floating wind turbine damping technology. Ocean Engineering 278: 114365. https://doi.org/10.1016/j.oceaneng.2023.114365

Wang CF, Chen JH, Wang ST, Fan ST, Ren H, Liu DH (2025) Sensitivity analysis and optimization of passive gyrostabilizers to mitigate pitch motion of a semi-submersible floating offshore wind turbine. Ocean Engineering 329: 121147. https://doi.org/10.1016/j.oceaneng.2025.121147

Xie SY, Li YR, He J, Kan YZ, Li YX (2025) Effect of nacelle motions on rotor performance and drivetrain dynamics in floating offshore wind turbines using fully coupled simulations. Journal of Marine Science and Application 24: 1150-1163. https://doi.org/10.1007/s11804-025-00636-1

Yang JJ, He EM (2020) Coupled modeling and structural vibration control for floating offshore wind turbine. Renewable Energy 157: 678-694. https://doi.org/10.1016/j.renene.2020.05.075

Yang XM, He L, Zhang RX, An LQ (2025) Mitigating wind-wave misalignment induced vibrations in semi-submersible offshore wind turbines using a 2D adjustable nonlinear tuned mass damper. International Journal of Structural Stability and Dynamics 2025: 2750006. https://doi.org/10.1142/S0219455427500064

Yu W, Lemmer F, Cheng PW (2023) Modeling and validation of a tuned liquid multi-column damper stabilized floating offshore wind turbine coupled system. Ocean Engineering 280: 114442. https://doi.org/10.1016/j.oceaneng.2023.114442

Zhang H, Wen BR, Tian XL, Li X, Dong YH, Wang MC, Peng ZK (2023) Experimental study on mitigating vibration of floating offshore wind turbine using tuned mass damper. Ocean Engineering 288: 115974. https://doi.org/10.1016/j.oceaneng.2023.115974

Zhang H, Wen BR, Tian XL, Li XF, Li X, Peng ZK (2025) Vibration reduction of floating offshore wind turbine with nonlinear vibration absorber: Concept, numerical analysis and experimental tests. Ocean Engineering 331: 121196. https://doi.org/10.1016/j.oceaneng.2025.121196

Zhang WZ, Calderon-Sanchez J, Duque D, Souto-Iglesias A (2024) Computational fluid dynamics (CFD) applications in floating offshore wind turbine (FOWT) dynamics: A review. Applied Ocean Research 150: 104075. https://doi.org/10.1016/j.apor.2024.104075

Zhang ZL (2022) Vibration suppression of floating offshore wind turbines using electromagnetic shunt tuned mass damper. Renewable Energy 198: 1279-1295. https://doi.org/10.1016/j.renene.2022.08.121

Zuo HR, Zhang J, Bi KM, Zhu SY, Hao H, Ma RS (2023) Structural vibration control of spar-buoy floating offshore wind turbines. Engineering Structures 294: 116732. https://doi.org/10.1016/j.engstruct.2023.116732